

UCSF

UC San Francisco Previously Published Works

Title

Self-assembled aldehyde dehydrogenase-activatable nano-prodrug for cancer stem cell-enriched tumor detection and treatment.

Permalink

<https://escholarship.org/uc/item/3623k9kd>

Journal

Nature Communications, 15(1)

Authors

Li, Bowen

Tian, Jianwu

Zhang, Fu

et al.

Publication Date

2024-10-31

DOI

10.1038/s41467-024-53771-8

Peer reviewed





Self-assembled aldehyde dehydrogenase-activatable nano-prodrug for cancer stem cell-enriched tumor detection and treatment

Received: 24 April 2024

Accepted: 23 October 2024

Published online: 31 October 2024

 Check for updates

Bowen Li^{1,3}, Jianwu Tian^{1,3}, Fu Zhang², Chongzhi Wu², Zhiyao Li², Dandan Wang¹, Jiahao Zhuang¹, Siqin Chen¹, Wentao Song¹, Yufu Tang¹, Yuan Ping²   & Bin Liu¹  

Cancer stem cells, characterized by high tumorigenicity and drug-resistance, are often responsible for tumor progression and metastasis. Aldehyde dehydrogenases, often overexpressed in cancer stem cells enriched tumors, present a potential target for specific anti-cancer stem cells treatment. In this study, we report a self-assembled nano-prodrug composed of aldehyde dehydrogenases activatable photosensitizer and disulfide-linked all-trans retinoic acid for diagnosis and targeted treatment of cancer stem cells enriched tumors. The disulfide-linked all-trans retinoic acid can load with photosensitizer and self-assemble into a stable nano-prodrug, which can be disassembled into all-trans retinoic acid and photosensitizer in cancer stem cells by high level of glutathione. As for the released photosensitizer, overexpressed aldehyde dehydrogenase catalyzes the oxidation of aldehydes to carboxyl under cancer stem cells enriched microenvironment, activating the generation of reactive oxygen species and fluorescence emission. This generation of reactive oxygen species leads to direct killing of cancer stem cells and is accompanied by a noticeable fluorescence enhancement for real-time monitoring of the cancer stem cells enriched microenvironment. Moreover, the released all-trans retinoic acid, as a differentiation agent, reduce the cancer stem cells stemness and improve the cancer stem cells enriched microenvironment, offering a synergistic effect for enhanced anti-cancer stem cells treatment of photosensitizer in inhibition of in vivo tumor growth and metastasis.

Tumor heterogeneity is an ongoing and formidable obstacle in cancer treatment due to a variety of cells in solid tumor bearing distinct phenotypic profiles with varying sensitivity to traditional therapies¹⁻³. Cancer stem cells (CSC) have been considered as a driving source of tumor heterogeneity, possessing a natural characteristic of stemness that induces self-renewal, multi-differentiation potential, and drug

resistance⁴⁻⁶. Clinical research has highlighted that CSC, characterized by their stemness, are different from normal cancer cells and yet similar to normal cells^{7,8}. This similarity lies in their quiescent and silent state, rendering them less susceptible to conventional anti-cancer treatments^{9,10}. Therefore, CSC-enriched tumor is insensitive to traditional chemotherapy or radiotherapy, which resulted in limited

¹Department of Chemical and Biomolecular Engineering, National University of Singapore, 4 Engineering Drive 4, Singapore 117585, Singapore. ²College of Pharmaceutical Sciences, Zhejiang University, Hangzhou 310058, China. ³These authors contributed equally: Bowen Li, Jianwu Tian.

 e-mail: pingsy@zju.edu.cn; cheliub@nus.edu.sg

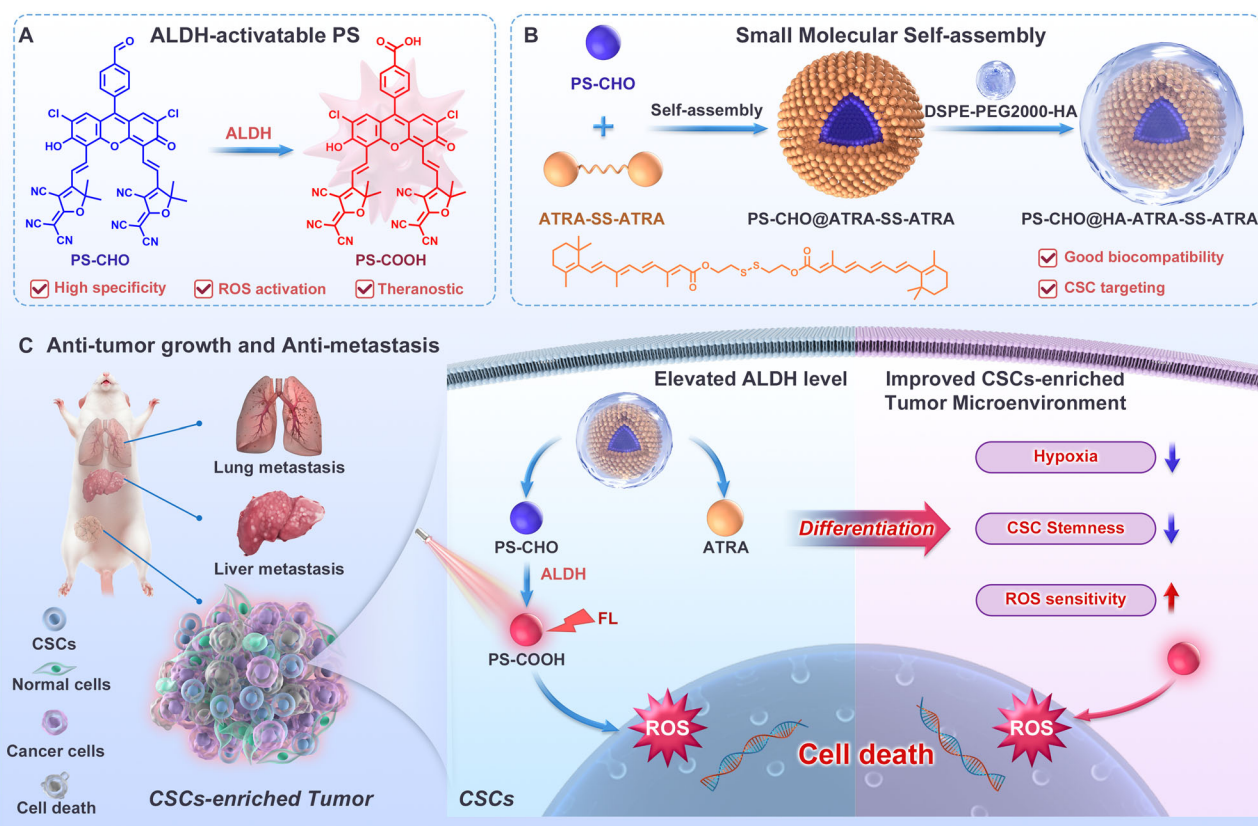


Fig. 1 Schematic illustration of overcoming traditional therapeutic obstacle of CSC-enriched tumor by aldehyde dehydrogenase-activatable nano-prodrug.

A The structure of PS-CHO and ALDH-responsive product PS-COOH. **B** The constitution and preparation of nano-prodrug PS-CHO@HA-ATRA-SS-ATRA. **C** The

targeted delivery, ALDH-responsiveness, synergistic effect and the inhibition of tumor growth and metastasis in CSCs-enriched tumor. Created in BioRender. Jiajing, G. (2024) BioRender.com/i52u535.

therapeutic effect^{11–13}. However, these residual CSC within lesion locations are often referred to as a “timebomb” due to their potential to undergo differentiation into mature cancer cells with elevated stemness, and this process can result in tumor metastasis and recurrence^{14–16}. Therefore, it is of practical importance to explore a specific and highly effective strategy for direct targeting and elimination of CSC-enriched tumors.

Through studying the unique stemness characteristics of CSC and their associated biomarkers, the overexpression of aldehyde dehydrogenase (ALDH) is found to be closely associated with poor survival rates in CSC-enriched tumors, including leukemia, pancreas, breast, and liver cancers^{17–21}. All these tumors often exhibit a high level of ALDH, which is considered as an important and specific biomarker in CSC-enriched tumor^{22,23}. In organisms, ALDH is an enzyme responsible for oxidizing xenobiotic aldehydes (-CHO) into the corresponding carboxylates (-COOH)^{24–26}. This unique enzymatic activity may provide a promising potential for designing ALDH-responsive prodrug with selective toxicity activation for the specific and safe treatment of CSC-enriched tumors.

Photodynamic therapy (PDT) has emerged as a promising non-invasive and highly efficient cancer treatment approach, utilizing reactive oxygen species (ROS) generated from photosensitizers (PSs) to induce cancer cell death^{27–29}. In comparison to traditional PSs, activatable PSs (aPSs) can be considered as PDT prodrugs, which remain inactive and non-toxic in their “OFF” state but transition to an “ON” state in response to specific stimuli present in the tumor microenvironment^{30–34}. This activation triggers ROS generation, leading to cell death in targeted tumor cells³⁵. Moreover, aPSs function as sensitive fluorescent probes, providing real-time information about

drug activation and tumor microenvironment^{36,37}. Therefore, the development of ALDH-responsive aPSs, capable of ROS generation and fluorescence monitoring in the CSC-enriched microenvironment, holds significant potential for the precise and high-efficiency treatment of CSC-enriched tumors.

Recent research has demonstrated that PDT can directly eliminate CSC-enriched tumors through ROS-induced cell apoptosis^{38,39}. However, prolonged or excessive use of apoptosis-related drugs, including PSs, may contribute to the enrichment of CSC stemness, leading to poor drug sensitivity and increased drug resistance^{4,40–42}. To address this challenge, differentiation therapy has been explored as an effective synergistic treatment to reduce CSC stemness and improve the CSC tumor environment, offering an indirect approach to decreasing CSC^{43–45}. Among various differentiation agents, all-trans retinoic acid (ATRA), an FDA-approved differentiation agent, has demonstrated significant efficacy in reducing CSC stemness in CSC-enriched tumors^{46,47}. However, ARTA has insignificant cytotoxicity against CSC and thus it is not effective for in vivo tumor inhibition in CSC-enriched tumor. Thus, the combination of ALDH-activatable PS and ATRA may integrate their advantage to overcome drug resistance of PDT and achieve a specific and high-efficiency therapeutic effect in CSC-enriched tumors.

In this work, we present a self-assembled nano-prodrug composed of an ALDH-responsive aPSs (PS-CHO) and the differentiation agent ATRA for precise and highly effective diagnose and PDT of CSC-enriched tumor. As shown in Fig. 1, PS-CHO contains an ALDH-responsive aldehyde group (-CHO) resulting in a weak PDT effect and low fluorescent signal. ATRA, conjugated with disulfide bond (-SS-) to form ATRA-SS-ATRA, demonstrates good self-assembly behavior^{48–50},

allowing it to load the hydrophobic PS-CHO and create a nan-prodrug (PS-CHO@ATRA-SS-ATRA). Under high ALDH expression, PS-CHO is transformed into PS-COOH, activating the PS-CHO and inducing cell death specifically through ROS generation. Moreover, the activation of PS-CHO also results in the restoration of its fluorescence signal, enabling real-time monitoring of the CSC-enriched microenvironment. In PS-CHO@ATRA-SS-ATRA, ATRA-SS-ATRA not only acts as a good carrier for PS-CHO but is also triggered by a high level of GSH to release ATRA. The released ATRA can reduce the stemness of CSC and improve the CSC-enriched microenvironment, offering a synergistic effect for enhanced anti-CSC treatment of PS-CHO. For targeted CSC-enriched tumor, PS-CHO@ATRA-SS-ATRA is decorated with hyaluronic acid (DSPE-PEG2000-HA), which specifically targets CD44 receptors highly expressed on CSC⁵¹. The systematic administration of PS-CHO@HA-ATRA-SS-ATRA has demonstrated good tumor-specific accumulation in different CSC-enriched tumor mice models, resulting in significant inhibition of tumor growth and minimized tumor metastasis in normal tissues, particularly in the lung and liver. The current study presents a proof-of-concept for a CSC-activated PDT prodrug with the adjuvant differentiation therapy, offering a precise and safe approach for treating various CSC-enriched cancers.

Results

Synthesis and characterization of PS-CHO and ATRA-SS-ATRA

The synthetic route of PS-CHO and ATRA-SS-ATRA is depicted in Fig. 2a-i. In general, compound **1** was synthesized according to the previous literature⁵², and then the -COOH on compound **1** was reduced to -CH₂OH (compound **2**) in 78.1% yield. Then, compound **2** was modified with -CHO by Duff reaction to offer compound **3** in 91.2% yield. Reaction between compound **3** and malonitrile derivatives by aldol reaction yielded compound **4**, which was oxidized to give PS-CHO (compound **5**) in 24.4% yield. In addition, the small molecular self-assembly prodrug ATRA-SS-ATRA (compound **6**) was obtained from ARTA upon reaction with 2,2'-disulfide diethanol by using 4-dimethylaminopyridine (DMAP)/triphosgene in 82.0% yield (Fig. 2a-ii). Meanwhile, we also obtained PS-COOH according to the previous literature⁵². All these compounds were confirmed by ¹H/¹³C nuclear magnetic resonance (¹H/¹³C NMR) and electro spray ionization-mass spectroscopy (ESI-MS) (Supplementary Figs. 1-14) to reveal their right structure and high purity.

ALDH-responsive behavior and ROS generation of PS-CHO in physiological conditions

ALDH is an enzyme responsible for the oxidation of aldehydes to carboxylic acids *in vivo*. Therefore, the ALDH-responsiveness of PS-CHO was first assessed by the qualitative analysis of ESI-MS. As shown in Supplementary Fig. 15, a new ionic peak emerged at 817.13 [M + H]⁺ after incubation with ALDH, which was assigned to PS-COOH. Moreover, the qualitative analysis of ALDH-responsiveness was also investigated by high-performance liquid chromatography (HPLC). As shown in Fig. 2b, the retention time of PS-CHO was emerged at 5.06 min. After incubation with ALDH, the intensity of PS-CHO was decreased, while a new retention time was observed at 2.78 min for PS-COOH. In addition, quantitative analysis of PS-CHO in high level of ALDH was also performed by HPLC. In Supplementary Fig. 16, the cumulative percentage of PS-COOH reached 50.7% in PBS solution (10% DMSO, due to poor solubility of PS-CHO in PBS solution) after 4 h incubation, and this relatively moderate transformation rate may be caused by poor water solubility of PS-CHO. All these results suggested that ALDH could effectively oxidize PS-CHO to PS-COOH under physiological conditions.

We next investigated the fluorescence properties of PS-CHO with or without ALDH. As shown in Fig. 2c, PS-CHO showed a relatively weak fluorescent signal at 778 nm when excited at 550 nm. After incubation with ALDH, an obvious fluorescence enhancement was observed at

767 nm, which gradually increased with time and reached a plateau in 4 h (Fig. 2d and Supplementary Fig. 17a). The higher ALDH concentration also triggered higher fluorescence intensity at 767 nm (Supplementary Figs. 17b and 18), which belonged to PS-COOH. In addition, the specificity of ALDH to PS-CHO was also evaluated *in vitro*. Only ALDH could induce significant fluorescence enhancement of PS-CHO, and the signal is stable over pH 4 to 10 (Supplementary Fig. 19a, b). Inspired by the good ALDH-responsive behavior of PS-CHO in physiological conditions, we next assessed the ROS generation under high ALDH microenvironments using a ROS probe (dichlorodihydrofluorescein, DCFH). In Fig. 2e and Supplementary Fig. 20, DCFH solution incubated with free PS-CHO displayed no obvious fluorescence enhancement at 525 nm under light irradiation, indicating its poor ROS generation capacity. However, a significant fluorescence enhancement was detected in PS-CHO after incubation with ALDH, indicating that ROS production capability was activated after the reaction. Additionally, the ROS generation of PS-CHO + ALDH increased with longer irradiation time (Fig. 2f).

Hypoxia is one of most important natural characteristics of the CSC microenvironment, which can inhibit the therapeutic effects of traditional type-II PSs due to their generate toxic singlet oxygen (¹O₂) via oxygen-dependent type-II photosensitizing process⁵³. Recently, emerging evidence has shown that Type-I PSs provide an effective and safe strategy to overcome this limitation of traditional PDT treatment. Type-I PSs are induced by electron transfer between the triplet states of excited PSs and surrounding substrates (such as lipids and proteins), leading to the formation of various ROS species such as superoxide anion (⁻O₂⁻), with relatively low oxygen concentration dependence^{54,55}. Therefore, we investigated the mechanism of ROS generation by the activated PS-CHO (PS-COOH) to determine whether it belongs to Type-I or Type-II PSs. As illustrated in Supplementary Fig. 21a, b, the fluorescence intensity of dihydrodrhodamine 123 (type I PS indicator for ⁻O₂⁻) in PS-CHO was increased by 33.1-fold after incubation with ALDH, significantly surpassing the enhancement observed with PS-CHO and PS-COOH alone. On the other hand, under light irradiation, PS-CHO with or without ALDH demonstrated low ¹O₂ generation using 9',10'-anthracenediyl-bis(methylene) dimalonate (ABDA) as the Type II PS indicator, consistent with the poor ¹O₂ production of PS-COOH (Supplementary Fig. 21c, d). Collectively, these results indicate that PS-COOH is a Type-I PS, which is promising for effective PDT treatment in hypoxic tumor microenvironments.

As PS-CHO is a hydrophobic molecule with poor water solubility, PS-CHO-based nano-formulation by ATRA-SS-ATRA was used to improve the biocompatibility. The small molecular self-assembly behavior of ATRA-SS-ATRA was first assessed by dynamic light scattering (DLS) and transmission electron microscopy (TEM). As shown in Supplementary Fig. 22, the nanoparticles of ATRA-SS-ATRA displayed spherical morphology with an obvious good size distribution (average size: 143 nm) and a low polydispersity index (PDI: 0.115). The DLS revealed that the nanoparticles have slightly negative surface charge (ζ potential: -0.178 mV, Supplementary Fig. 23). Based on this finding, the nano-formulation of PS-CHO (nano-prodrug, PS-CHO@ATRA-SS-ATRA) was prepared by nanoprecipitation with ATRA-SS-ATRA (Fig. 2g). DLS and TEM results indicate that PS-CHO@ATRA-SS-ATRA has an average size of 166.4 nm (PDI: 0.129) with an obvious Tyndall effect (Fig. 2h, i) and display spherical morphology with the positive ζ potential (8.78 mV) (Supplementary Fig. 23). Moreover, the drug loading efficiency (DLE) of PS-CHO in PS-CHO@ATRA-SS-ATRA was determined by HPLC to be about 52.1%. The stability was also investigated by DLS, and the size distribution and PDI remained stable after 30 days of storage (Supplementary Fig. 24a, b). In addition, due to the presence of -SS- in ATRA-SS-ATRA, PS-CHO@ATRA-SS-ATRA disassembled after incubation with 10 mM GSH (Supplementary Fig. 25). This GSH-responsive disassembly

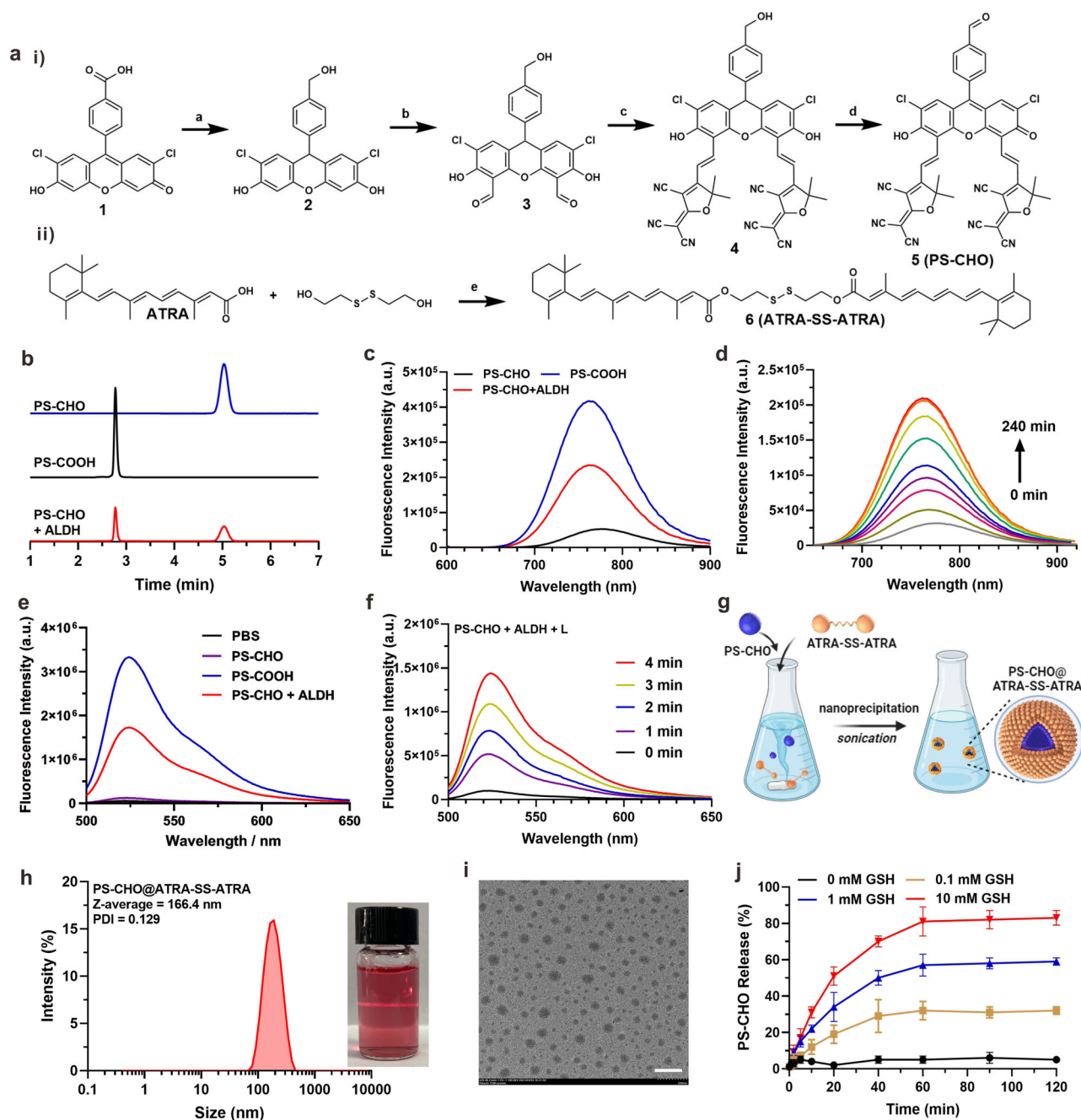


Fig. 2 | The synthesis of PS-CHO and ATRA-SS-ATRA, ALDH-responsiveness of PS-CHO and Preparation of PS-CHO@ATRA-SS-ATRA. **a** The synthesis route of PS-CHO and ATRA-SS-ATRA. The condition and agents: **a**. NaBH₄, I₂, 60 °C; **b** Hexamethylenetetramine, CF₃COOH, 80 °C; **c** Et₃N, 2-(3-cyano-4,5,5-trimethylfuran-2(SH)-ylidene) malononitrile; **d** Dess-Martin Reagent. r.t.; **e** DCC, DMAP, 0-r.t., overnight. **b** The HPLC profiles for PS-CHO, PS-COOH and PS-CHO treated with ALDH (50 μg/mL) in PBS for 4 h. **c** Fluorescence spectra of PS-CHO, PS-COOH and PS-CHO incubated with ALDH (50 μg/mL) for 4 h. **d** Fluorescence variation PS-CHO incubated with ALDH (50 μg/mL) at different times (0–4 h). **e** Total ROS generation for PBS, PS-CHO, PS-COOH and PS-CHO with ALDH

(50 μg/mL) by DCFH assay (40 mW/cm², 4 min). **f** Total ROS generation for PS-CHO with ALDH (50 μg/mL) at different times (0–4 min) by DCFH assay (White light: 40 mW/cm², 4 min). **g** The preparation of PS-CHO@ATRA-SS-ATRA. Created in BioRender. Jiajing, G. (2023) BioRender.com/u78h472. **h** The size distribution of PS-CHO@ATRA-SS-ATRA by DLS. **i** The morphology of PS-CHO@ATRA-SS-ATRA by TEM. Scale bar: 500 nm. **j** Cumulative PS-CHO release rate from PS-CHO@ATRA-SS-ATRA incubated with different concentration of GSH (0, 0.1, 1 and 10 mM) by HPLC. (*n* = 3 independent samples; means ± SD). All enzymatic reactions were performed in PBS solution (0.1 M, pH 7.4) containing NAD(H)⁺ (1 mM).

behavior could also induce PS-CHO release from nanoparticles, and the PS-CHO release behavior was investigated by HPLC. With the increasing GSH concentrations, PS-CHO@ATRA-SS-ATRA progressively released PS-CHO and reached a maximum cumulative release of 83.1 % after 4 h incubation (Fig. 2j). Meanwhile, a similar drug release rate of ATRA (77.8 %) was also detected in Supplementary Fig. 26. The above results indicated that high level of GSH

could trigger disassembly behavior, further releasing both PS-CHO and ATRA under physiological conditions.

Intracellular ALDH-responsive behavior and ROS generation of PS-CHO@ATRA-SS-ATRA

We first investigated the ALDH-responsive behavior of small molecular PS-CHO and nano-prodrug PS-CHO@ATRA-SS-ATRA by fluorescence

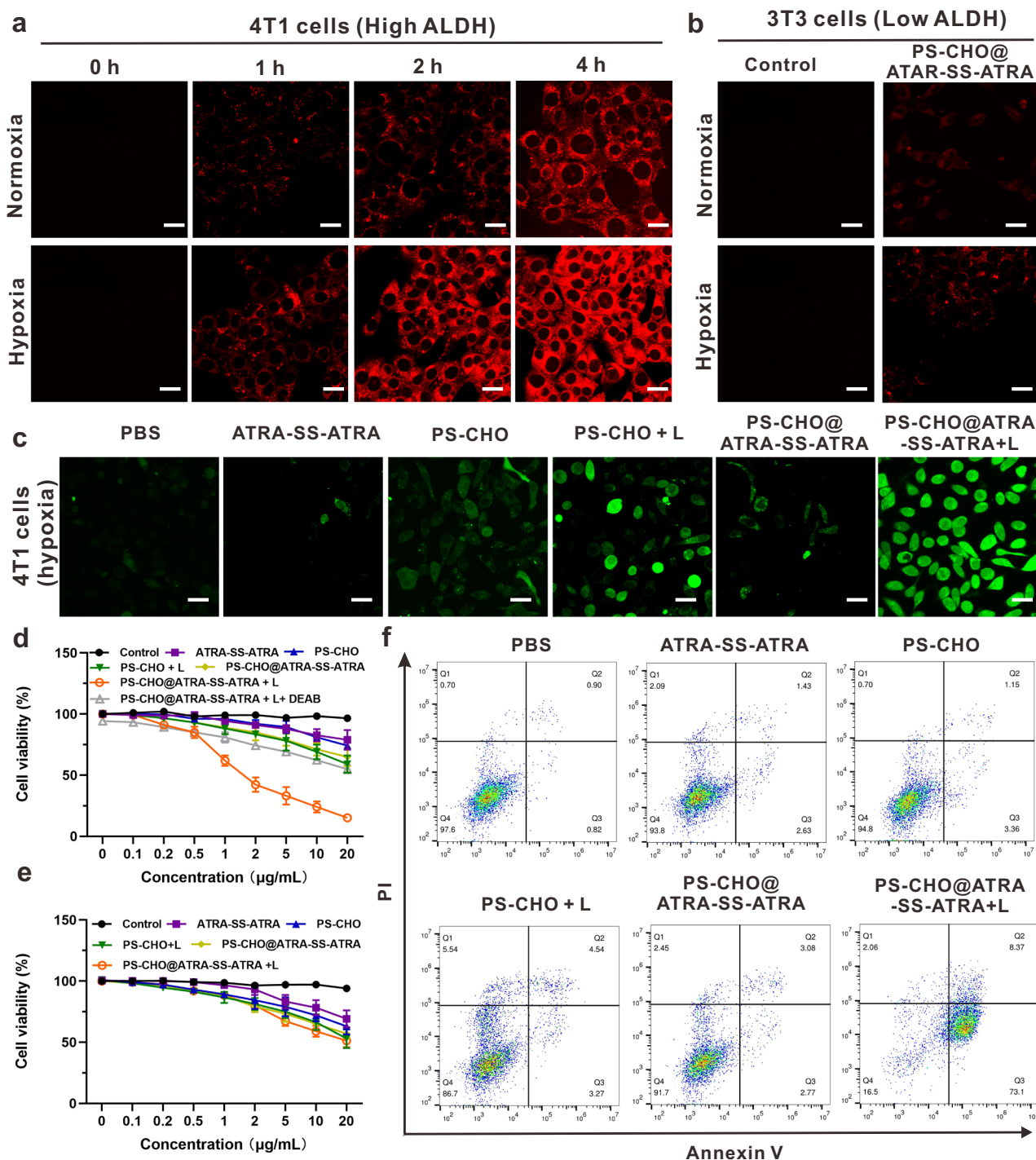


Fig. 3 | The ALDH-responsive, ROS generation and cytotoxicity of PS-CHO@ATRA-SS-ATRA. **a** Confocal images of 4T1 cells treated with PS-CHO@ATRA-SS-ATRA with different times (0, 1, 2 and 4 h) under hypoxia and normal condition. Scale bar: 20 µm. **b** Confocal images of 3T3 cells treated with PS-CHO@ATRA-SS-ATRA under hypoxia and normal condition. Scale bar: 20 µm. **c** Confocal imaging of 4T1 cells treated with PS-CHO@ATRA-SS-ATRA by light irradiation, and then incubated with DCFH-DA for intracellular ROS generation.

Scale bar: 20 µm. **d** The cytotoxicity of different formulations to 4T1 cells ($n = 6$ independent biological samples; means \pm SD). **e** The cytotoxicity of different formulations to 3T3 cells ($n = 6$ independent biological samples; means \pm SD). **f** The apoptosis analysis of 4T1 cells incubated with different formulations was stained by Annexin V and PI and measured using flow cytometry. L: white light: 40 mW/cm², 4 min.

imaging in CSC-enriched 4T1 cells. As shown in Supplementary Fig. 27, no obvious fluorescent signal was detected in small molecular PS-CHO dissolved in 1% DMSO for cell experiments due to its poor solubility, while there was a strong fluorescent signal in the nano-prodrug PS-CHO@ATRA-SS-ATRA. Recently, solid evidence proved that hypoxia microenvironment is a typical characteristic of CSC-enriched

microenvironment, which could induce the higher expression of ALDH and upregulate the CSC-enriched microenvironment. Based on these findings, we evaluated the ALDH-responsive behavior in 4T1 cells under hypoxic condition. As shown in Fig. 3a and Supplementary Fig. 28, the fluorescence intensity of PS-CHO@ATRA-SS-ATRA was stronger under hypoxic condition due to the elevated level of ALDH,

and this intensity was gradually increased in a time- and dose-dependent manner, providing a real-time reporting of CSC-enriched microenvironment.

As a control, there was no obvious fluorescent signal in 3T3 cells (normal cells) under hypoxic conditions, indicating the low side-effect of PS-CHO@ATRA-SS-ATRA in normal cells (Fig. 3b). Based on the good ALDH-responsive activation and high-efficiency drug release behavior of PS-CHO@ATRA-SS-ATRA in CSC-enriched 4T1 cells, we next investigated its ROS generation by using a ROS probe (DCFH-DA) as the indicator. In 4T1 cells, a weak green fluorescence was detected in ATRA-SS-ATRA, free PS-CHO and PS-CHO@ATRA-SS-ATRA without light irradiation, and PS-CHO with light irradiation also displayed a poor green fluorescence due to the poor cell uptake. In contrast, the nano-prodrug, PS-CHO@ATRA-SS-ATRA, exhibited much stronger fluorescence in 4T1 cells after light irradiation, suggesting that the high level of ALDH could transform PS-CHO into PS-COOH and thus trigger the ROS generation (Fig. 3c). In normal cells, only faint fluorescence was detected in all formulations, suggesting that our nano-prodrug was not able to produce ROS and therefore exhibited good biosafety (Supplementary Fig. 29). To further confirm ALDH-responsive fluorescence and ROS generation, *N,N*-diethylaminobenzaldehyde (DEAB) was used as an ALDH inhibitor for the control experiments. As shown in Supplementary Fig. 30a, a strong red fluorescence was observed in 4T1 cells after incubation with PS-CHO@ATRA-SS-ATRA, while an obvious decline of red fluorescence was detected in 4T1 cells pretreated with DEAB. This decline is due to the inhibition of ALDH, which prevents the transformation of PS-CHO into PS-COOH. Similarity, a noticeable reduction in ROS generation was also observed in 4T1 cells pretreated with DEAB (Supplementary Fig. 30b).

Cytotoxicity of PS-CHO@ATRA-SS-ATRA

Inspired by the good ROS activation of PS-CHO@ATRA-SS-ATRA on CSC-enriched cancer cells, we next performed CCK8 assays in different types of cells to evaluate whether the ALDH-responsive behavior of PS-CHO could result in potential cytotoxicity. In both CSC-enriched cancer cells (4T1) and no-CSC normal cells (3T3), free ATRA-SS-ATRA, PS-CHO and PS-CHO@ATRA-SS-ATRA displayed very low cytotoxicity without light irradiation, and PS-CHO with light irradiation also showed relatively low cytotoxicity due to the poor cell uptake (Fig. 3d, e). In contrast, PS-CHO@ATRA-SS-ATRA with light irradiation exhibited high cytotoxicity in 4T1 cells but poor toxicity in 3T3 cells, which was due to its good selectivity, as well as good cell uptake by ALDH-responsive activation and the improvement of water solubility. Moreover, PS-CHO@HA-ATRA-SS-ATRA showed low cytotoxicity to DEAB-treated 4T1 cells (Fig. 3d). As shown in Supplementary Fig. 31, PS-CHO@HA-ATRA-SS-ATRA also showed strong cytotoxicity towards other CSC-enriched cancer cells (e.g. MDA-MB-231 and OE21), but negligible cytotoxicity towards normal cells (e.g. 3T3 and L929). These findings highlight the selective toxicity of the nano-prodrug towards CSC cancer cells, underscoring its potential as a targeted therapy for CSC-enriched tumors. In addition, flow cytometry analysis and LIVE/DEAD cell death assay indicated that free ATRA-SS-ATRA, free PS-CHO and PS-CHO@ATRA-SS-ATRA merely induced any cell death, and relatively low cell death was observed in free PS-CHO with light irradiation. Under the same condition, PS-CHO@ATRA-SS-ATRA showed the highest level of cell death (Fig. 3f and Supplementary Fig. 32), suggesting that PS-CHO@ATRA-SS-ATRA could induce high cytotoxicity of CSC-enriched cancer cells due to ALDH-responsive activation.

In vitro elimination and differentiation of CSC on CSC-related tumor spheres

The cell cytotoxicity suggested that PS-CHO@ATRA-SS-ATRA showed good therapeutic efficacy on CSC-enriched cancer cells. To further confirm the good CSC elimination of PS-CHO@ATRA-SS-ATRA, we

successfully constructed the CSC-enriched 4T1 tumor sphere model, which could mimic the in vivo CSC-enriched microenvironment. In 4T1 tumor sphere model, the CSC elimination and CSC-enriched microenvironment were mainly investigated by four key indicators, including tumorsphere formation, hypoxia conditions (HIF-1 α), ALDH-positive cell proportions (ALDH⁺), and stemness-related gene (*Sox2*, *Nanog* and *Oct4*). To assess the synergic effect of ATRA, the nano-prodrug without ATRA (PS-CHO@DSPE-PEG2000, Supplementary Fig. 33) was also prepared by loading PS-CHO with DSPE-PEG2000 and serve as a negative control. As shown in Supplementary Fig. 27, the cell uptake of PS-CHO@DSPE-PEG2000 was determined by fluorescence imaging and flow cytometry, and the qualitative and quantitative analysis revealed that the fluorescence intensity of PS-CHO@DSPE-PEG2000 was similar to that of PS-CHO@ATRA-SS-ATRA, suggesting similar cell uptake of PS-CHO@DSPE-PEG2000 and PS-CHO@ATRA-SS-ATRA by 4T1 cells.

As tumorspheres have been used to determine the percentage of CSC present in a tumor population, and thus it also used for evaluating the ability of such cells to generate stemness, and the numbers of tumorspheres can be used to visualize the effectiveness of anti-CSC treatment^{56–58}. In Fig. 4a, b, a large amount and volume of tumorspheres was observed in control group and free PS-CHO, suggesting insignificant CSC elimination. In addition, all ATRA-contained formulations exhibited smaller and lower dispersive tumorspheres, because ATRA could provide an effective differentiation-inducing effect to reduce the stemness of CSC, further improving CSC-enriching environment. As control, PS-CHO@DSPE-PEG2000 with light irradiation also reduced the number and volume of tumor spheres and further inhibited tumorsphere formulation, indicating that PS-CHO@DSPE-PEG2000 could be effectively triggered by ALDH and transformed into activated PSs (PS-COOH) for eliminating CSC. It was also observed that PS-CHO@ATRA-SS-ATRA with light irradiation displayed stronger inhibition of tumorsphere formulation than that of PS-CHO@DSPE-PEG2000, which was contributed to the improvement of CSC-enriched microenvironment from ATRA (Fig. 4a). The elevated stemness of CSC could sharply reduce the oxygen concentration in the CSC-enriched microenvironment, which upregulated the expression of hypoxia-inducible factors (HIFs)^{59,60}. Therefore, HIFs can serve as an important indicator for the CSC stemness and numbers of CSC formulation. Based on this finding, CSC elimination was also investigated by HIF-1 α expression of 4T1 tumorspheres. The HIF-1 α was labeled by green dye and cell nuclei were stained with blue dye (Hoechst). As shown in Fig. 4c, a strong green fluorescent signal was observed for the control group and free PS-CHO without light irradiation, and there was a much weaker green fluorescent signal in the formulation contained ATRA or PS-CHO with light irradiation, especially in PS-CHO@ATRA-SS-ATRA. All these results suggested that both ATRA and PS-CHO could effectively eliminate the CSC and further induce the downregulation of HIF-1 α , achieving the improvement of therapeutic effects on CSC-enriched microenvironments.

ALDH is known as a CSC biomarker, and the higher proportions of ALDH positive (ALDH⁺) cancer cells are usually associated with the stronger CSC-enriched microenvironment⁶¹. After treatment with our nano-prodrug, the CSC elimination was monitored by the proportions of ALDH⁺ in 4T1 tumorspheres. As shown in Fig. 4d, PBS (negative control) exhibited high proportions of ALDH⁺ (26.7%) in 4T1 tumorspheres, and the similar results were also detected in free PS-CHO without light irradiation (25.19%). In ATRA-contained formulation, the proportions of ALDH⁺ were decreased to 16.33% and 15.98% due to the differentiation-inducing effect of ATRA. As control, PS-CHO@DSPE-PEG2000 with light irradiation showed lower proportions of ALDH⁺ (8.39%) than that of ATRA-contained formulation, which was due to good elimination of CSC by ALDH-activated PDT treatment. Among

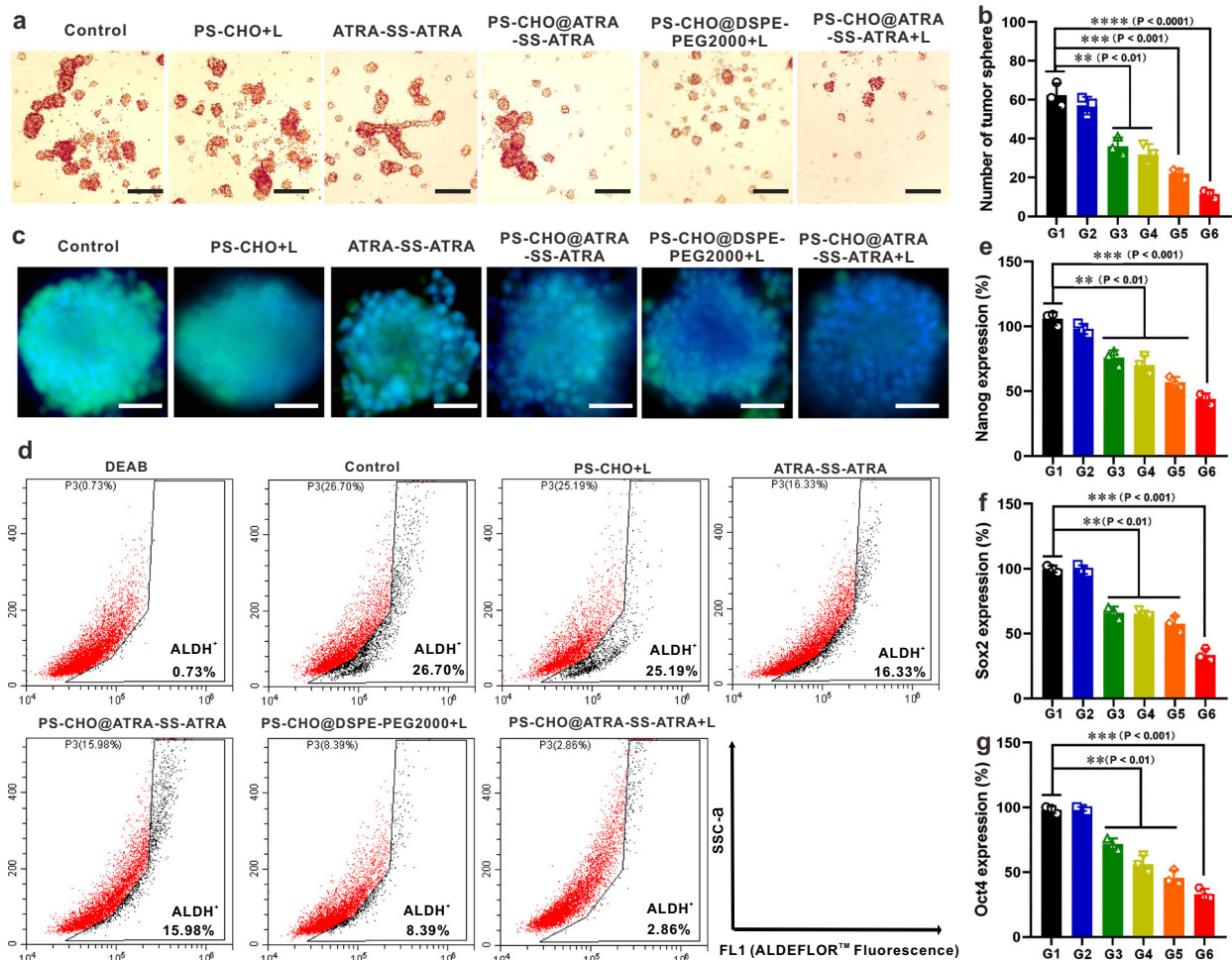


Fig. 4 | In vitro differentiation-inducing ability of nano-prodrug. **a** The images of 4T1 cells in tumor-sphere formation assay after different drug treatments. Scale bar: 500 μ m. **b** The tumor-sphere formation numbers after different drug treatments ($n = 3$ independent biological samples; means \pm SD). **c** The images of immunofluorescence for detecting the HIF-1 α expression of 4T1 tumor-sphere cells after different drug treatments. Nuclei were stained by DAPI. Scale bar: 100 μ m. **d** The proportions of ALDH⁺ cells in 4T1 tumor-sphere cells after different

drug treatments measured by flow cytometry. **e–g** The stemness-related genes (*Sox2*, *Nanog* and *Oct4*) of 4T1 tumor-sphere cells after different treatments quantified by qPCR ($n = 3$ independent biological samples; means \pm SD). L: white light (40 mW/cm², 4 min). The statistical significance is analyzed by one-way ANOVA with a Tukey post hoc test. ** $p < 0.01$, *** $p < 0.001$, and **** $p < 0.0001$. Saline (G1), PS-CHO + L (G2), ATRA-SS-ATRA (G3), PS-CHO@ATRA-SS-ATRA (G4), PS-CHO@DSPE-PEG2000 + L (G5), and PS-CHO@ATRA-SS-ATRA + L (G6).

these formulations, PS-CHO@ATRA-SS-ATRA displayed the lowest proportions of ALDH⁺ (2.86%) that was close to ALDH inhibitor (DEAB, 0.73%, positive control). Finally, the stemness-related genes (*Sox2*, *Nanog* and *Oct4*) were also evaluated by 4T1 tumorsphere model. As shown in Fig. 4e–g, all ATRA-contained formulation exhibited an obvious decline of *Sox2*, *Nanog* and *Oct4* gene expression, indicating good improvement of CSC-enriched microenvironment. As expected, PS-CHO@ATRA-SS-ATRA exhibited highest down-regulation of *Sox2*, *Nanog* and *Oct4* genes in all formulations, further confirming that the ALDH-activated nano-prodrug could effectively eliminate the CSC and reduce the CSC-enriched microenvironment.

Preparation and in vitro drug release behaviors of nano-prodrug PS-CHO@ATRA-SS-ATRA and CSC-targeting nano-prodrug PS-CHO@HA-ATRA-SS-ATRA

To further enhance drug accumulation of the CSC-enriched tumor and maintain high stability in systemic circulation, we decorated a layer of hyaluronic acid (HA) with DSPE-PEG2000 (DSPE-PEG2000-HA) on the surface of PS-CHO@ATRA-SS-ATRA to render active CSC targeting capability. After coating, DLS suggested that the hydration diameter of PS-CHO@HA-ATRA-SS-ATRA slightly increased from 166.4 nm to

188.6 nm with a low PDI (0.129), which was also confirmed by TEM (Fig. 5a, b). The ζ potential was decreased from 8.78 mV to -17.7 mV (Supplementary Fig. 23), and the DLE (PS-CHO) in PS-CHO@HA-ATRA-SS-ATRA was about 29.3%. Moreover, PS-CHO@HA-ATRA-SS-ATRA demonstrated good physical stability in different media, including PBS, FBS, and plasma (Supplementary Fig. 34), and showed a similar release profile to that of the PS-CHO@ATRA-SS-ATRA (Supplementary Fig. 35).

To confirm that HA coating enhances cell uptake in CSC-enriched 4T1 cells, we selected an anti-CD44 antibody as a strong ligand to block the CD44 receptor on the surface of CSC. As shown in Supplementary Figs. 36 and 37, PS-CHO@HA-ATRA-SS-ATRA exhibited higher ALDH responsiveness and ROS generation than that of PS-CHO@ATRA-SS-ATRA in CSC-enriched 4T1 cells, while distinctly reducing in 4T1 cells pretreated with anti-CD44 antibody. These results indicate that the HA coating increases CSC uptake of PS-CHO@HA-ATRA-SS-ATRA, mediated by the CD44 receptor, which is overexpressed on the surface of CSC. In contrast, PS-CHO@HA-ATRA-SS-ATRA exhibited low level of ALDH responsiveness and ROS generation in A549 and 3T3 cells (low ALDH) (Supplementary Figs. 36 and 37). Similar results were observed in the cytotoxicity of different nano-formulations, with PS-CHO@HA-

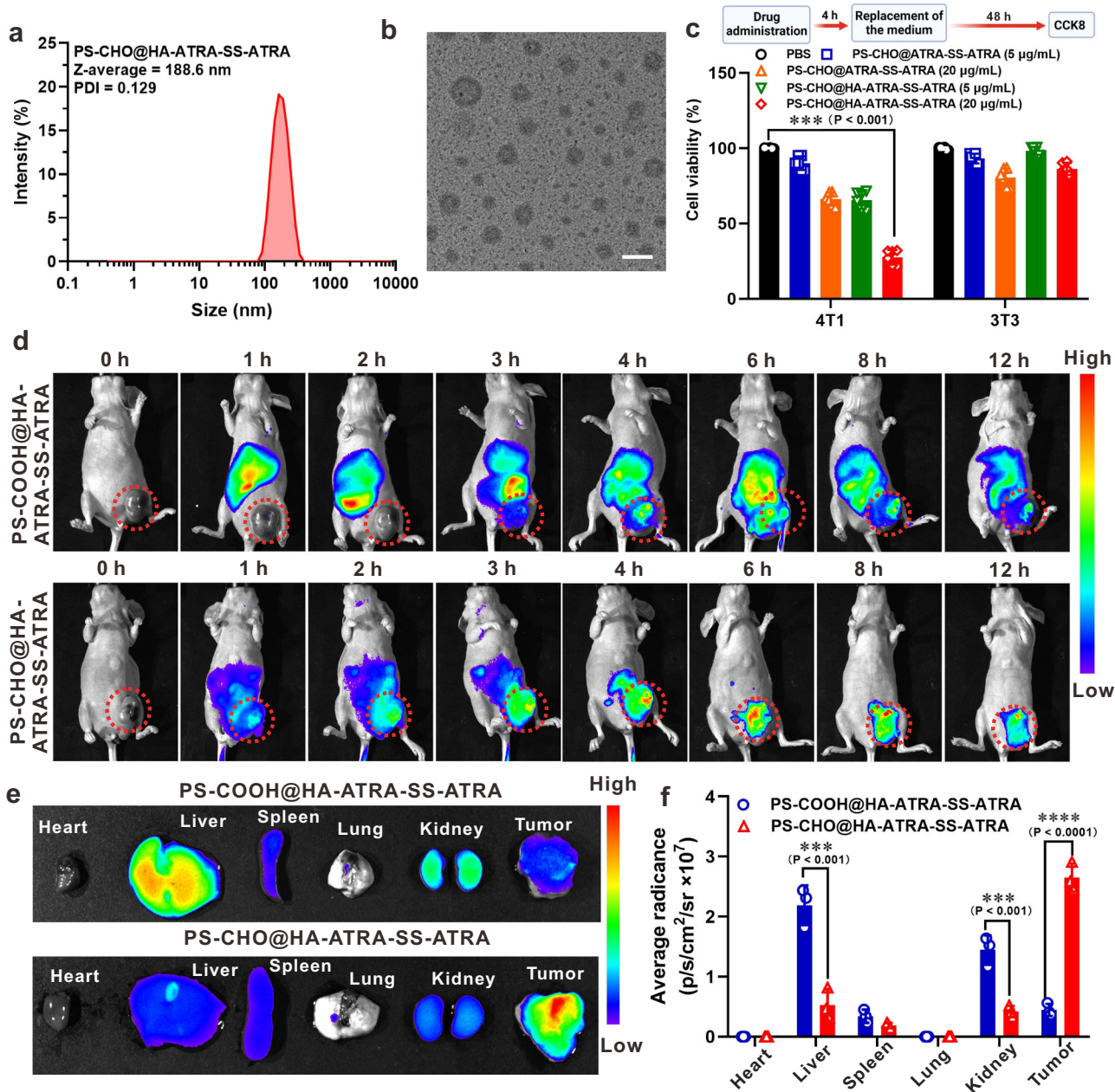


Fig. 5 | Preparation of CSC-targeting nano-formulations PS-CHO@HA-ATRA-SS-ATRA and in vivo drug release. **a** The size distribution of PS-CHO@HA-ATRA-SS-ATRA by DLS. **b** The morphology of PS-CHO@HA-ATRA-SS-ATRA by TEM. Scale bar: 200 nm. **c** Cell viability of 4T1 and 3T3 cells incubated PS-CHO@HA-ATRA-SS-ATRA and PS-CHO@ATRA-SS-ATRA based on short-term drug administration (white light :40 mW/cm²; 4 min) ($n = 6$ independent biological samples; means \pm SD). **d** In vivo fluorescence images of 4T1 subcutaneous mice after intravenous

injection of PS-CHO@HA-ATRA-SS-ATRA and PS-CHO@ATRA-SS-ATRA at pre-determined time intervals until 12 h post-administration. The red dashed lines indicated the tumor areas. **e, f** Ex vivo fluorescence images of tumor and main organs (heart, liver, spleen, lung and kidney) resected from the mice at 12 h post-administration ($n = 3$ independent biological samples; means \pm SD). The statistical significance is analyzed by one-way ANOVA with a Tukey post hoc test, *** $p < 0.001$ **** $p < 0.0001$.

ATRA-SS-ATRA exhibiting the highest cytotoxicity against 4T1 cells among all formulations tested (Supplementary Fig. 38). Moreover, a short-term drug administration was investigated by CCK8 assay. As shown in Fig. 5c, both 4T1 and 3T3 cells were first treated with PS-CHO@ATRA-SS-ATRA or PS-CHO@HA-ATRA-SS-ATRA for 4 h, and then the medium was replaced with fresh medium for another 48 h. As compared with PS-CHO@ATRA-SS-ATRA, PS-CHO@HA-ATRA-SS-ATRA could induce higher cytotoxicity in 4T1 cells, while very low cytotoxicity was observed in 3T3 cells when PS-CHO@HA-ATRA-SS-ATRA concentration was high, owing to the good CSC targeting in CSC-enriched cancer cells.

In vivo ALDH-responsiveness of PS-CHO@HA-ATRA-SS-ATRA

We first evaluated the hemocompatibility of our nano-prodrug, as shown in Supplementary Fig. 39. Small molecular PS-CHO displayed relatively poor hemocompatibility that the hemolysis rate is over 20% due to poor water solubility, whereas the nano-formulations that contained DSPE-PEG2000-HA showed the lowest hemolysis rate (less than 2%), indicating that the poor biocompatibility of small molecular PS-CHO. Subsequently, the in vivo drug release was detected by IVIS imaging system, and the ALDH-activated PS-COOH could serve as a fluorescent dye for monitoring drug distribution. In Fig. 5d, an obvious fluorescent signal was detected on tumor site after 1 h

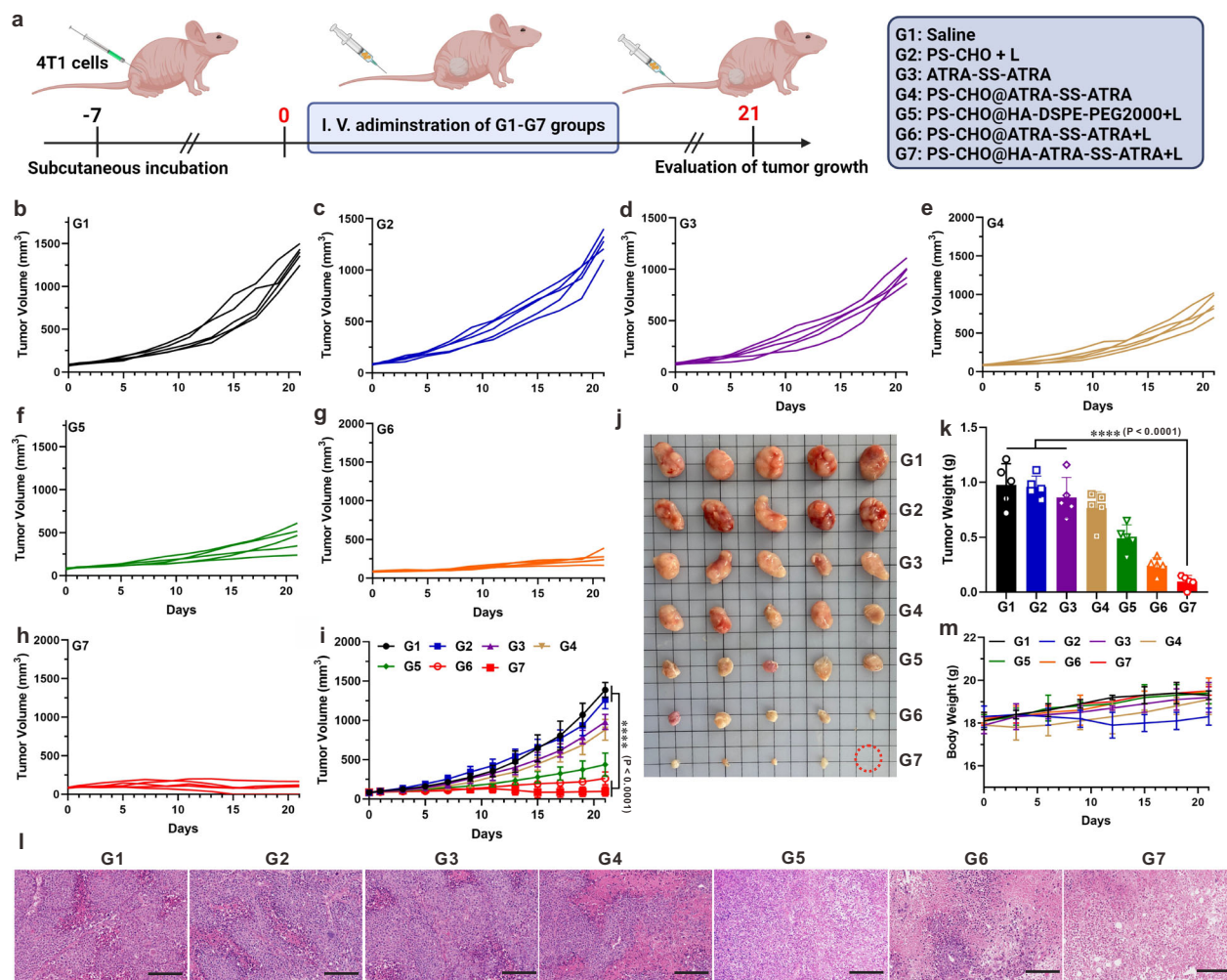


Fig. 6 | In vivo anti-tumor efficacy on a CSC-enriched subcutaneous model.

a Process of the in vivo efficacy study in 4T1-subcutaneous mice model, and all mice were intravenously administered by G1-G7 groups. Created in BioRender. Jijiang, G. (2023) [BioRender.com/v30s379](https://www.biorender.com/v30s379). **b-h** Tumor growth of subcutaneous 4T1 tumor-bearing mice after G1-G7 treatments. **i** Tumor volume growth of each mouse from G1-G7 groups at the end of 21 days treatment ($n = 5$ independent biological samples; means \pm SD). **j** Photograph of excised tumors from G1-G7 groups at the end of 21 days treatment. **k** Average tumor weight excised from G1-G7 groups at the end of 21 days treatment ($n = 5$ independent biological samples; means \pm SD). **l** H&E

staining of the tumor tissues from G1-G7 groups after different treatments. Scale bar: 200 μ m. **m** The changes in body weights of subcutaneous 4T1 tumor-bearing mice in G1-G7 groups within 21 days ($n = 5$ independent biological samples; means \pm SD). L: white light (60 mW/cm², 5 min). The statistical significance is analyzed by one-way ANOVA with a Tukey post hoc test, **** $p < 0.0001$. Saline (G1), PS-CHO + L (G2), ATRA-SS-ATRA (G3), PS-CHO@ATRA-SS-ATRA (G4), PS-CHO@HA-DSPE-PEG2000 + L (G5), PS-CHO@ATRA-SS-ATRA + L (G6), and PS-CHO@HA-ATRA-SS-ATRA + L (G7).

intravenous injection of PS-CHO@HA-ATRA-SS-ATRA, which increased with time and remained strong after 12 h injection. In main organs, we only observed some fluorescent signals at liver site after the first 3 h injection, whereas there was no obvious signal in other sites at the period of 12 h injection (Fig. 5d). As a positive control, PS-COOH was also transformed into the HA-modified nanoparticle (PS-COOH@HA-ATRA-SS-ATRA, Supplementary Fig. 40) that displayed “always on” fluorescent signal. In Fig. 5d, we found that a stronger fluorescent signal was first detected in the liver, and then gradually accumulated in the abdomen site. Note that the fluorescent signal in liver and abdomen site gradually increased to the highest 6 h after the systemic administration and then maintained stable. At tumor site, an obvious fluorescent signal was visible at 4 h and became strong at 6 h, but this fluorescent signal was much lower than that of PS-CHO@HA-ATRA-SS-ATRA. This result indicated that PS-CHO@HA-ATRA-SS-ATRA mainly triggered PS-CHO in tumor site that might display good biosafety. Moreover, the mice were sacrificed to obtain the main organs for ex vivo imaging after 12 h injection, as shown in Fig. 5e, f, PS-CHO@HA-ATRA-SS-ATRA exhibited the strongest fluorescent signal on tissue,

whereas PS-COOH@HA-ATRA-SS-ATRA was mainly distributed in metabolic organ (such as liver and kidney), which may cause potential phototoxicity and other side effects. These encouraging results illustrated the advantage of ALDH-responsiveness of PS-CHO@HA-ATRA-SS-ATRA, which was mainly activated on the CSC-enriched tumor and displayed good therapeutic effect by high selectivity and good biosafety.

In vivo anti-tumor efficiency on a 4T1 subcutaneous model

Inspired by good tumor accumulation and effective ALDH-responsiveness of our nano-prodrug, we further investigated their effects in tumor treatment (Fig. 6a). Compared with Saline (G1, Fig. 6b), systemic administration of ATRA-SS-ATRA (G3) and PS-CHO@ATRA-SS-ATRA without light irradiation (G4) exhibited negligible inhibition of tumor growth after 21-days treatment (Fig. 6d, e). Small molecular PS-CHO with light irradiation (G2) also exhibited poor tumor growth inhibition (Fig. 6c), whereas the nano-formulation of PS-CHO without ATRA, PS-CHO@HA-DSPE-PEG2000 that PS-CHO modified with DSPE-PEG2000-HA (G5, Supplementary Fig. 41), could obviously inhibit the

tumor growth (Fig. 6f). On the other hand, PS-CHO@ATRA-SS-ATRA with light irradiation (G6) exhibited some better tumor growth inhibition than that of G5, which was contributed to the synergistic therapeutic effect of ATRA (Fig. 6g). As expected, the CSC-targeted nano-prodrug PS-CHO@HA-ATRA-SS-ATRA (G7) resulted in almost complete response of tumor growth (Fig. 6h), and most tumors in mice were reduced greatly and even faded away. The summarized analysis in Fig. 6i also revealed the best tumor inhibition of G7. On 21 days, all mice were sacrificed and dissected to collect tumor tissue and main organs, and the photograph and weight of dissected tumor tissues also revealed that G7 displayed the best tumor growth inhibition in all groups (Fig. 6j, k). Moreover, similar results were also proved by H&E staining of ex vivo tumor tissues, and there was an obvious histological damage in the tumor tissue after the treatment of G7 (Fig. 6l). As shown in Fig. 6m and Supplementary Fig. 42, no obvious loss in body weight and no obvious histological damage in the main organs were observed after G7 treatment, indicating the safe profile of this CSC-targeted nano-prodrug. As a result, mice with G7 treatment exhibited the highest tumor growth inhibition and better biosafety during a period of 21-day treatment.

In vivo anti-tumor efficiency and anti-metastasis on a TNBC-orthotopic mice model

Clinic research revealed the aggressive nature of TNBC, characterized by higher rates of distant metastasis and recurrence, is influenced by the residual CSC in TNBC tumor⁶². This small subpopulation of CSC within TNBC plays a critical role in initiating and driving the metastatic process, often affecting sites like the lungs, liver, and bones⁶³. Therefore, we further investigated the anti-tumor growth and anti-metastatic effect of PS-CHO@HA-ATRA-SS-ATRA on TNBC-orthotopic mice model (Fig. 7a). After 30 days treatment, there was no obvious difference of tumor growth in Saline (G1, control group), PS-CHO with light irradiation (G2), ATRA-SS-ATRA (G3), and PS-CHO@ATRA-SS-ATRA without light irradiation (G4) (Fig. 7b and Supplementary Fig. 43a-d). Especially in G2, small molecular PS-CHO with light irradiation displayed poor tumor inhibition due to its poor biocompatible, while the nano-formulations of PS-CHO with light irradiation (G5: PS-CHO@HA-DSPE-PEG2000; G6: PS-CHO@ATRA-SS-ATRA, and G7: PS-CHO@HA-ATRA-SS-ATRA) can effectively suppress the tumor growth after 30-days treatment (Fig. 7b and Supplementary Fig. 43e, f). As compared with G5 and G6 groups, much stronger inhibition was observed in tumor growth after CSC-targeted nano-prodrug (G7) treatment (Fig. 7b and Supplementary Fig. 43g). On day 30, all mice were sacrificed and dissected to obtain the tumor tissues and main organ, and tumor weight and photograph of different groups revealed the similar results of in vivo tumor inhibition (Fig. 7c, d). In addition, the anti-tumor efficacy was also confirmed by H&E staining, as shown in Supplementary Fig. 44, nano-prodrug G5 (without ARTA) and G6 (without HA targeting) groups exhibited obvious histological damage in tumor tissues, indicating good inhibition by the effective ALDH-responsive PDT treatment. As control, nano-prodrug G7 group (contained HA and ATRA) showed the deepest histological damage in all groups due to effective synergic effect of ATRA and good CSC-targeting of HA.

In clinics, the distant metastasis from TNBC is often diagnosed at lung and liver, which was a leading cause of death in TNBC treatment. Therefore, we investigated the inhibition of distant metastases on the TNBC-orthotopic mice model by different immunohistochemical staining. In lung tissue, the Bouin's fluid was first stained to mark the lung metastatic nodules, and fewer metastatic nodules were observed for all nano-formulation groups, while other groups displayed more obvious lung nodules. In comparison with G1-G4, the nano-formulation G5 was able to effectively inhibit the distant metastases on the surface of lung tissue. Both G6 and G7

exhibited the poorest metastatic nodules, especially for targeted nano-prodrug that the number of lung nodules was negligible with less than 5 lung metastases per mouse, suggesting a strong anti-metastasis effect of G7 (Fig. 7e). Furthermore, only a few nodules were detected after PS-CHO@HA-ATRA-SS-ATRA treatment (Fig. 7f), which was confirmed by H&E staining, suggesting the effective inhibition of lung metastasis. In the liver tissue, the H&E staining was performed to investigate its distant metastatic nodule, as shown in Fig. 7g, an obvious tumor metastatic nodule was observed in G1-G4 groups, while there was no obvious metastatic nodule in G7, and this result was similar with that of lung metastases.

To confirm the good anti-CSC effect of our nano-prodrug, we analyzed the ALDH-expression of tumor tissue by immunofluorescence staining. As shown in Fig. 7h, G1, G2, G3 and G4 showed relatively strong green, fluorescent signal in tumor tissues. As a control, G5 also displayed relatively poor fluorescent signal in tumor tissue, which was due to PS-CHO@HA-DSPE-PEG2000 could effectively accumulate into CSC and then activate PS-CHO to kill the CSC. As expected, the tumor tissues treated with nano-formulation G6 and G7 (simultaneously contained ATRA and PS-CHO) hardly observed green fluorescence, indicating fewer ALDH-overexpressed CSC in tumor microenvironment. In addition, the expression of stemness-related genes (*Sox2*, *Nanog* and *Oct4*) in tumor tissues was also investigated after different groups treatment. As shown in Supplementary Fig. 45, G7 was able to effectively down-regulate the expression of stemness-related gene and decrease the generation of CSC. Collectively, these results suggested that reduced CSC in tumor tissue were able to effectively inhibit distant metastasis in vivo. During the treatment period of 30 days, although G2 (free PS-CHO) caused slow growth in body weight, there were no obvious changes in other groups, including G7 (Supplementary Fig. 46). In addition, there was no obvious histological damage in the main organs after the treatment of G7 (Supplementary Fig. 47). After G7 treatment, 80% of mice survived for 60 days, indicating the long-term anti-metastatic effect. The above results proved that our nano-prodrug exhibited good biosafety and could prolong the survival rate of mice with distant metastatic foci (Supplementary Fig. 48).

Discussion

We have explored a simple and convergent self-assembled nano-prodrug containing an ALDH-activatable PS and differentiation agents ATRA for CSC-associated tumor treatment. The ALDH-activatable PS (PS-CHO) exhibited good ALDH-responsiveness with triggered ROS activation and fluorescence generation in vitro. To improve the biocompatibility and in vivo therapeutic effect, ATRA was linked with -SS-bond to form a GSH-response ATRA-SS-ATRA, which exhibited good small molecular self-assembly behavior, serving as a good nano-carrier to load PS-CHO. The PS-CHO@ATRA-SS-ATRA not only effectively enhanced the pharmacokinetics of PS-CHO due to its good water dispersibility but also reduced CSC stemness and improved the CSC-enriched tumor microenvironment by the synergistic effect of ATRA. In CSC-enriched tumor cells, PS-CHO@ATRA-SS-ATRA disassembled into PS-CHO and ATRA by high level of GSH, and PS-CHO was transformed into PS-COOH under high expression of ALDH that generated the fluorescence for reporting the real-time information about the CSC microenvironment. Moreover, PS-COOH exhibited good ROS generation that can directly eliminate CSC and indirectly improve CSC-enriched microenvironment. More importantly, such distinct anti-CSC mechanism of two drugs satisfies the demand for promoting a maximized synergistic effect in CSC-enriched mice model, exhibiting the good inhibition of tumor growth and metastasis. These findings provide a promising perspective for exploring simple, convergent, and effective strategies to improving the therapeutic effect in a wide range of CSC-enriched tumors.

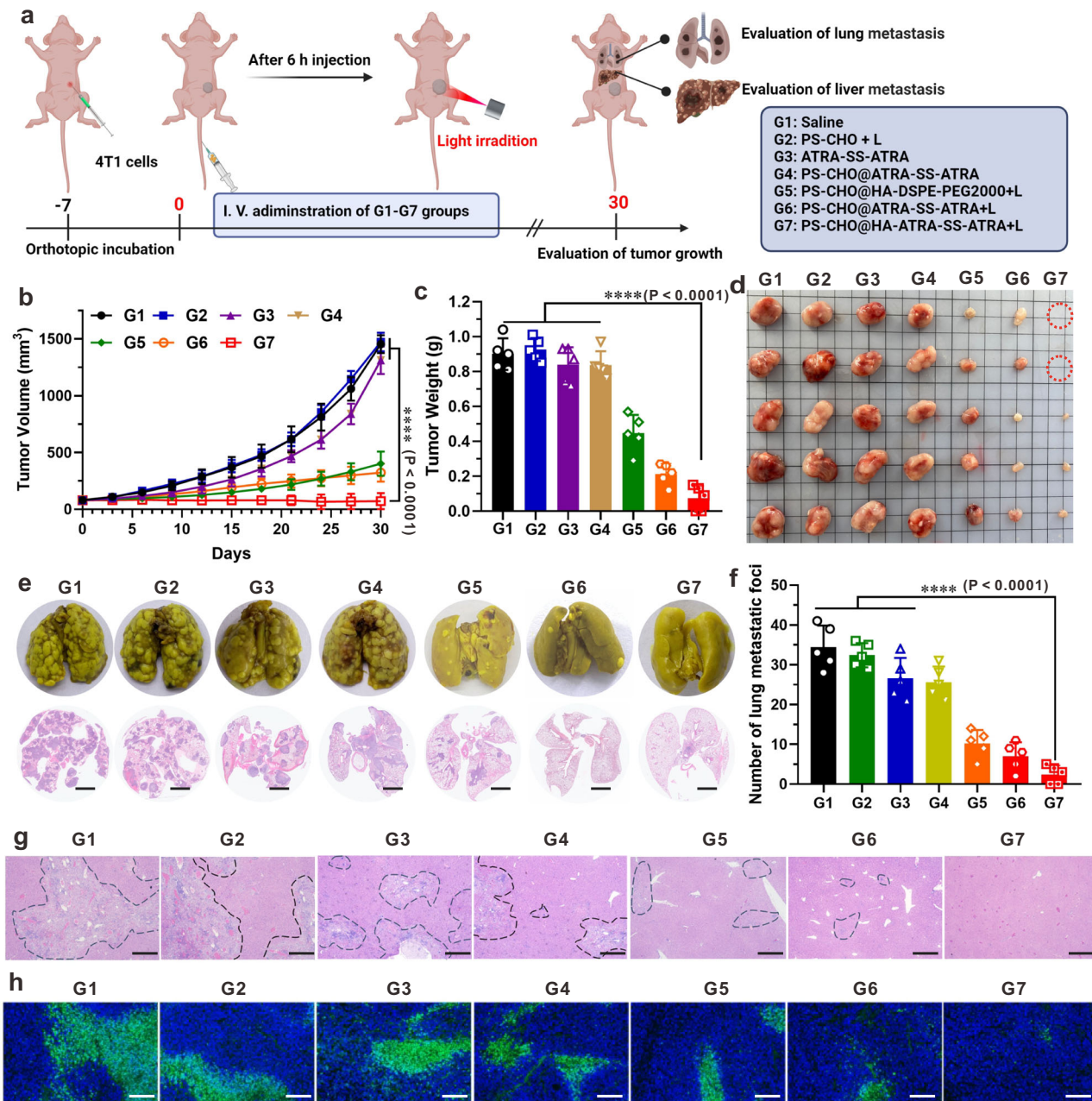


Fig. 7 | In vivo tumor growth inhibition and anti-metastasis on a CSC-enriched orthotopic mice model. **a** Process of the in vivo efficacy study in 4T1-orthotopic mice model, and all mice were intravenously administered by G1-G7 groups. Created in BioRender. Jiajing, G. (2023) BioRender.com/v30s379. **b** Tumor growth of each mouse in different groups ($n = 5$ independent biological samples; means \pm SD). **c** The average tumor weight excised from G1-G7 groups ($n = 5$ independent biological samples; means \pm SD). **d** Photograph of the dissected tumor tissues of G1-G7 groups. **e** Representative H&E and Bouin's Fluid staining images (lung metastasis) of lung tissue excised from G1-G7 groups on day 30. Scale bar: 5 mm. **f** Quantification

of lung metastatic foci from G1-G7 groups on day 30. ($n = 5$ independent biological samples; means \pm SD). **g** Representative H&E staining images (metastatic foci) of liver tissue excised from G1-G7 groups on day 30. Scale bar: 200 μm . **h** Representative ALDH immunofluorescence staining images of tumor tissue excised from G1-G7 groups on day 30. L: white light (60 mW/cm^2 , 5 min). The statistical significance is analyzed by one-way ANOVA with a Tukey post hoc test, **** $p < 0.0001$. Saline (G1), PS-CHO + L (G2), ATRA-SS-ATRA (G3), PS-CHO@ATRA-SS-ATRA (G4), PS-CHO@HA-DSPE-PEG2000 + L (G5), PS-CHO@ATRA-SS-ATRA + L (G6), and PS-CHO@HA-ATRA-SS-ATRA + L (G7).

Methods

Preparation and synthesis of nanoparticles PS-CHO@ATRA-SS-ATRA and PS-CHO@HA-ATRA-SS-ATRA

The nanoparticles PS-CHO@ATRA-SS-ATRA were prepared by nanoprecipitation, and small molecular PS-CHO (5 mg) and ATRA-SS-ATRA (5 mg) were added into dimethyl sulfoxide (DMSO, 1 mL) and then slowly injected to 19.5 mL of ddH₂O under vigorous sonication (-10 min). This crude product of PS-CHO@ATRA-SS-ATRA was loaded with dialysis tube (MWCO = 1000 Da) and then dialyzed for

12 h in ddH₂O. As for PS-CHO@HA-ATRA-SS-ATRA, PS-CHO (2 mg), ATRA-SS-ATRA (2 mg) and DSPE-PEG2000-HA (1 mg) were added into DMSO (0.5 mL) and then slowly added to 9.5 mL of ddH₂O under vigorous sonication (-10 min) and then dialyzed for 12 h in ddH₂O (MWCO = 5000 Da).

The nanoparticles PS-CHO@DSPE-PEG2000 and PS-CHO@HA-DSPE-PEG2000 were also prepared by nanoprecipitation. The DMSO solution of PS-CHO (5 mg, 1 mL) was slowly added into 19 mL ddH₂O containing 1 mg of DSPE-PEG2000-HA or DSPE-PEG2000, and this

solution was mixed under sufficient stirring. This crude product was subjected to dialysis (MWCO = 2000 Da) against ddH₂O to remove the DMSO and the residual drug.

The drug loading efficiency (DLE) of PS-CHO in PS-CHO@ATRA-SS-ATRA and PS-CHO@HA-ATRA-SS-ATRA was determined by high-performance liquid chromatography (HPLC). The precipitate of PS-CHO@ATRA-SS-ATRA and PS-CHO@HA-ATRA-SS-ATRA was collected, dried and weighed. Then, the dried nanoparticle (10 mg) was dissolved in DMSO and quantitatively analyzed the weight of PS-CHO by HPLC. The DLE was calculated according to the following formula:

$$\text{DLE}_{(\text{PS-CHO})} = [(\text{Weight of PS-CHO}) / (\text{Weight of nanoparticle})] \times 100\% \quad (1)$$

ALDH-responsive behavior of PS-CHO in PBS solutions

All enzymatic reactions were performed according to the reported literature^{17,24}. ALDH was diluted with PBS (0.1 M, pH 7.4) to make a buffered solution of ALDH at different concentrations. 10% DMSO as cosolvent of prodrug was mixed with a PBS solution (0.1 M, pH 7.4) containing nicotinamide adenine dinucleotide (NAD(H)⁺, 1 mM). For ALDH-responsive assays, the above solution was added ALDH solution (50 µg/mL) and performed at 37 °C. The ALDH-responsive behavior of PS-CHO was first investigated by HPLC, which was performed by C18 column under 25 °C condition. The mobile phase was methanol and water at the ratio of 9:1. The PS-CHO was first incubated with 50 µg/mL of ALDH for 1 h in PBS cosolvent solution, and then it was analyzed by HPLC. In addition, the ALDH-responsive behavior of PS-CHO was also detected by fluorescence imaging, PS-CHO, PS-COOH and PS-CHO incubated with ALDH were dissolved in PBS cosolvent solution under 37 °C, and the fluorescence spectra were measured by fluorescence spectrometer. For different concentrations (0–100 µg/mL) or times (0–240 min), PS-CHO (20 µg/mL) was incubated with different concentrations (0–100 µg/mL) for 2 h or with 50 µg/mL of ALDH for different times. Finally, the ALDH-responsive behavior of PS-CHO was also detected by HR-MS. The PS-CHO (20 µg/mL) was first incubated with 50 µg/mL of ALDH in PBS cosolvent solution, and after 1 h incubation, the mixture was analyzed by HR-MS.

ROS generation of PS-CHO in PBS solutions

A commonly used ROS indicator DCFH-DA was utilized to detect the ROS generation in an aqueous solution under white light irradiation. The general procedure is as follows: DCFH-DA was pre-hydrolyzed into DCFH, and then this ROS indicator was further diluted to 10 µM in PBS solution (0.1 M, pH 7.4) of 20 µg/mL of PS-CHO, PS-CHO with ALDH and PS-COOH. The fluorescence of DCFH triggered by ROS under white light irradiation was measured at different time intervals. The fluorescence spectra were measured with excitation at 488 nm and emission was collected from 500 to 600 nm. The fluorescence intensity at 525 nm was recorded to indicate the generation rate of overall ROS. The ·O₂ generation was assessed by employing DHR123 as an indicator. 20 µg/mL of PS-CHO, PS-CHO with ALDH and PS-COOH was incubated with DHR123 solution, which was irradiated by white light (40 mW/cm²) for 4 min, and then emission spectra of DHR123 were monitored in a range of 500–600 nm. The emission increase of DHR123 at 525 nm was recorded to indicate the generation rates of ·O₂. The ¹O₂ generation was assessed by employing ABDA as an indicator. 20 µg/mL of PS-CHO, PS-CHO with ALDH and PS-COOH was incubated with ABDA solution, which was irradiated by white light (40 mW/cm²) for 4 min, and then the absorption spectra of ABDA were monitored in a range of 300–500 nm. The absorbance decrease of ABDA at 378 nm was recorded to indicate the decomposition rates of ABDA.

In vitro drug release behavior

The nanoparticle PS-CHO@ATRA-SS-ATRA (20 µg/mL) was incubated with different level of GSH (0–10 mM), which then extracted and

detected by HPLC using C18 column under 25 °C condition, and the mobile phase was methanol and water at the ratio of 9:1. In detail, 2 mL of each sample was added into a 500 Da dialysis bag and dialyzed against PBS (0.1 M, pH 7.4) with different concentration of GSH (0–10 mM) at 37 °C in a shaker. At predetermined time intervals (0, 1, 2, 5, 10, 20, 30, 60 and 120 min), 1 mL solution in each sample was taken out and 1 mL of fresh PBS was restored its solutions. The concentration of PS-CHO was measured by HPLC.

Intracellular ALDH-responsive behavior in normal and cancer cells

The intracellular ALDH-responsive behavior of PS-CHO@ATRA-SS-ATRA was investigated by cell imaging in different cells (normal cells: 3T3, cancer cells: A549 and 4T1) under hypoxic and normal environment. All these cells were added into 8-well confocal plate under normal or hypoxic conditions, allowing for suitable growth density (60%). Then, PS-CHO@ATRA-SS-ATRA was added into plates by the different concentration (0, 5, 10, and 20 µg/mL) or different time (0–4 h, at the concentration of 10 µg/mL), and then incubated for another 4 h. After PBS (0.1 M, pH 7.4) washing, the intracellular fluorescence intensity was recorded by using CLSM. The ALDH-responsive behavior of PS-CHO@DSPE-PEG2000 (10 µg/mL) and PS-CHO@HA-ATRA-SS-ATRA (10 µg/mL), and the protocol was the same with the ALDH-responsive behavior of PS-CHO@ATRA-SS-ATRA.

Intracellular ROS detection

The ROS generation of different formulations was investigated by ROS indicator (DCFH-DA). Different cells (normal cells: 3T3, cancer cells: A549 and 4T1) were seeded in 8-well plates, allowing for suitable growth density (70%) under hypoxic condition. After the cell adhesion, different formulations (ATRA-SS-ATRA, PS-CHO, PS-CHO + L, PS-CHO@ATRA-SS-ATRA and PS-CHO@ATRA-SS-ATRA + L, 20 µg/mL) were added and incubated for 24 h. Then, all treated cells were washed by PBS (0.1 M; pH 7.4) for 3 times and then irradiated with or without laser. For ROS generation of PS-CHO@HA-ATRA-SS-ATRA + L, the protocol was the same with the ROS generation of PS-CHO@ATRA-SS-ATRA + L. All these cells were stained by DCFH-DA for 30 mins and observed in a fluorescent microscope. L: white light (40 mW/cm², 4 min).

Blockage of CD44 in CSC-enriched cells

CSC-enriched 4T1 cells were cultured in 8-well confocal plates under hypoxic condition. After their reach to 80% confluence. Anti-CD44 primary antibody (Abcam, ab189524) was diluted 1:200 in PBS solution (0.1 M, pH 7.4) and added into cells for blocking CD44. After the incubation of 2 h., this CD-44 blocking cells were incubated with PS-CHO@HA-ATRA-SS-ATRA (20 µg/mL), and ALDH-responsive behavior and ROS generation was recorded according to the above protocol.

In vitro cytotoxicity

Different cells (normal cells: 3T3, cancer cells: 4T1) were added into 96-well plates (100 µL, 5000 cells for each well). After the cell adhesion, a gradient concentration (0–20 µg/mL) of different formulations (PBS, ATRA-SS-ATRA, PS-CHO, PS-CHO + L, PS-CHO@ATRA-SS-ATRA, PS-CHO@ATRA-SS-ATRA + L and PS-CHO@HA-ATRA-SS-ATRA + L) were added and incubated for 48 h, and all the cells were irradiated with white light (40 mW/cm²) for 5 min, using the ones without light illumination as the control. Then, all treated cells were washed by PBS (0.1 M, pH 7.4) and added 10 µL of CCK-8 solution (diluted in 200 µL PBS). After 4 h incubation at 37 °C, the absorption values at 450 nm were measured by a UV-vis instrument. The cell viability was determined by comparison with the PBS groups. As for short-term drug administration, different cells were firstly incubated with different concentrations (5 and 20 µg/mL) of PS-CHO@ATRA-SS-ATRA + L and PS-CHO@HA-ATRA-SS-ATRA + L for 4 h and then replaced with fresh medium and continue to incubate for another 48 h. Finally, the CCK8

assay was performed according to the standard protocol. For the control experiment, 4T1 cells were first incubated with ALDH inhibitor DEAB for 4 h, and then incubated with PS-CHO@ATRA-SS-ATRA + L at a gradient concentration (0 - 20 $\mu\text{g}/\text{mL}$) for 48 h. The cytotoxicity was performed by CCK8 assays according to the standard protocol. For other CSC-enriched cancer cells (MDA-MB-231 and OE21) and normal cells (L929), the concentration (20 $\mu\text{g}/\text{mL}$) of PS-CHO@HA-ATRA-SS-ATRA + L, and the protocol of cytotoxicity was the same with CCK8 assays. L: white light (40 mW/cm^2 ; 4 min).

Cell death by Live/dead Staining

4T1 cells were added in 24-well plates (500 μL , 5×10^4 cells for each well). After the cell adhesion, different drug formulations (PBS, ATRA-SS-ATRA, PS-CHO, PS-CHO + L, PS-CHO@ATRA-SS-ATRA, and PS-CHO@ATRA-SS-ATRA + L, 20 $\mu\text{g}/\text{mL}$) were added and incubated for 4 h. Then, all treated cells were irradiated with white light irradiation (40 mW/cm^2) for 4 min. After another 24 h incubation, the cells were washed by PBS (0.1M; pH 7.4) and stained by Calcein-AM/PI for 30 mins. Then the cells were washed by PBS (0.1M; pH 7.4) and observed in a fluorescent microscope.

Cell apoptosis by Flow Cytometry Assay

4T1 cells were added in 6-well plates (2 mL, 2×10^5 cells for each well). After the cell adhesion, different drug formulations (PBS, ATRA-SS-ATRA, PS-CHO, PS-CHO + L, PS-CHO@ATRA-SS-ATRA, and PS-CHO@ATRA-SS-ATRA + L, 20 $\mu\text{g}/\text{mL}$) were added and incubated for 4 h, and then all treated cells were irradiated with or without white light irradiation (40 mW/cm^2) for 4 min. After 24 h incubation, the adherent and suspended cells were all collected and performed according to the protocol. After being stained by Annexin-V-FITC/PI in dark for 30 mins, the cells were performed by flow cytometry and measure the apoptosis rates. The gating strategy of the flow cytometry for apoptosis was provided in Supplementary Fig. 49a.

In vitro tumorspheres formation assay

4T1 cells were added in ultra-low adhesion 24-well plates (500 μL , 1×10^4 cells for each well) and incubated under hypoxic conditions. Then different drug formulations (PBS, PS-CHO + L, ATRA-SS-ATRA, PS-CHO@ATRA-SS-ATRA, PS-CHO@DSPE-PEG2000 + L and PS-CHO@ATRA-SS-ATRA + L) at the concentration of 20 $\mu\text{g}/\text{mL}$ were added and incubated for 5 days, the cells were observed and the numbers of tumorspheres were recorded by using microscope. L: white light (40 mW/cm^2 , 4 min).

ALDH-positive rate of tumorsphere cells

4T1 cells were added in ultra-low adhesion 24-well plates (500 μL , 1×10^4 cells for each well) and incubated under hypoxic conditions. Then different drugs (PBS, PS-CHO + L, ATRA-SS-ATRA, PS-CHO@ATRA-SS-ATRA, PS-CHO@DSPE-PEG2000 + L, and PS-CHO@ATRA-SS-ATRA + L) at the concentration of 20 $\mu\text{g}/\text{mL}$ were added and incubated for 3 days, all treated cells were collected and washed by PBS (0.1M, pH 7.4), and then stained with ALDEFLUOR kit for flow cytometry. The untreated cells were added with N, N-diethylaminobenzaldehyde (DEAB) to determine the ALDH-positive cells in other groups. L: white light (40 mW/cm^2 , 4 min). The gating strategy of the flow cytometry for ALDH-positive rate was provided in Supplementary Fig. 49b.

Stemness-related genes expression of tumorsphere cells

4T1 cells were added in ultra-low adhesion 24-well plates (500 μL , 1×10^4 cells for each well) and incubated under hypoxic conditions. Then different drugs (PBS, PS-CHO + L, ATRA-SS-ATRA, PS-CHO@ATRA-SS-ATRA, PS-CHO@DSPE-PEG2000 + L and PS-CHO@ATRA-SS-ATRA + L) at the concentration of 20 $\mu\text{g}/\text{mL}$ were added and incubated for 3 days, RNAs in the cells were extracted by an RNA extraction kit. The

stemness-related gene (*Sox2*, *Nanog* and *Oct4*) were quantified by qPCR analysis. L: white light (40 mW/cm^2 , 4 min).

HIF-1 α expression by immunofluorescence

4T1 cells were added in ultra-low adhesion 24-well plates (500 μL , 1×10^4 cells for each well) under hypoxic conditions and allowed for the tumorsphere formation. Then the tumorspheres were collected and transferred to 48-well plates (1 tumorsphere per well) and exposed to different drugs (PBS, PS-CHO + L, ATRA-SS-ATRA, PS-CHO@ATRA-SS-ATRA, PS-CHO@DSPE-PEG2000 + L and PS-CHO@ATRA-SS-ATRA + L) at the concentration of 20 $\mu\text{g}/\text{mL}$. After 3 days incubation, all treated cells were fixed with 4% paraformaldehyde and incubated with 0.5% Triton-X-100, and then washed with PBS for 3 times. Then, the tumorsphere cells were blocked by goat serum, and the incubated with the primary antibody of HIF-1 α at 4 °C overnight. After that these treated cells were incubated with Alexa Fluor 488 conjugated secondary antibodies for 1 h and the nucleus was stained by DAPI. The HIF-1 α expression was determined and observed by a fluorescent microscope. L: white light (40 mW/cm^2 , 4 min).

In vivo imaging and drug release behavior of PS-CHO@ATRA-SS-ATRA

The CSC-enriched subcutaneous tumor model was established by the injection of 4T1 cells, which were subcutaneously injected into the right groins of female BALB/c mice (5×10^5 4T1 cells, 6 weeks old). After the tumor volume reached about 500 mm^3 , different formulations (PS-CHO@HA-ATRA-SS-ATRA and PS-COOH@HA-ATRA-SS-ATRA) were performed by intravenous injection into the 4T1 subcutaneous tumor mice ($n = 3$). At several time intervals (0, 1, 2, 3, 4, 6, 8 and 12 h), the mice were subjected to in vivo imaging by IVIS system. After 12 h, the mice were sacrificed, and the tumors and organs (hearts, livers, spleens, lungs and kidneys) were collected for ex vivo imaging. The fluorescent signals were monitored through a 740 nm band-pass filter and excited by a 540 nm LED.

In vivo anti-tumor efficacy in a 4T1 subcutaneous model

The CSC-enriched subcutaneous tumor model was established by the injection of 4T1 cells, which were subcutaneously injected into the right groins of female BALB/c mice (5×10^5 4T1 cells, 6 weeks old). After the tumors reached about 100 mm^3 , the mice were randomly distributed into 7 groups ($n = 5$) (G1-G7: Saline, PS-CHO + L, ATRA-SS-ATRA, PS-CHO@ATRA-SS-ATRA, PS-CHO@HA-DSPE-PEG2000 + L, PS-CHO@ATRA-SS-ATRA + L and PS-CHO@HA-ATRA-SS-ATRA + L, 5 mg/kg), and then all groups were intravenously injected for three times on day 0, 3, and 6. After 12 h injection, the mice of G2, G5, G6, and G7 were irradiated by white light (60 mW/cm^2 , 5 min). At the period of 21-days, the tumor volume was recorded for each mouse every 2 days and then calculated according to $(\text{longest width}) \times (\text{longest length})^2/2$. The tumor volumes and body weights were recorded every 3 days. On day 21, all mice were sacrificed and dissected to obtain the tumor tissue and main organs. The tumors were weighted and made into slices for H&E and ALDH immunofluorescence staining. The organs were made into slices for H&E staining. Another batch of mice were received the same treatment for survival analysis until day 60.

In vivo anti-tumor efficacy and anti-metastasis in 4T1-orthotopic mice model

4T1 cells (5×10^6 cells/mL) were orthotopically injected into the right second mammary pad of female nude mice. After injection, all mice were randomly divided into 7 groups and intravenously injected G1-G7 groups (Saline, PS-CHO + L, ATRA-SS-ATRA, PS-CHO@ATRA-SS-ATRA, PS-CHO@HA-DSPE-PEG2000 + L, PS-CHO@ATRA-SS-ATRA + L and PS-CHO@HA-ATRA-SS-ATRA + L, 5 mg/kg) for three times on day 0, 3, and 6. After 12 h injection, the mice of G2, G5, G6, and G7 were irradiated by white light (60 mW/cm^2 , 5 min). At the period of 30-days, the tumor

volume was recorded for each mouse every 3 days, which were calculated according to $(\text{longest width}) \times (\text{longest length})^2/2$. At 30 days, all mice were sacrificed and dissected to obtain the tumor tissue and main organs. In addition, the body weight of all groups was also recorded at the treatments of 30-days. For tumor inhibition and intratumoral ALDH expression, the tumor tissues of all groups were stained by H&E staining of stemness-related genes (*Sox2*, *Nanog* and *Oct4*). For the distant metastases, the lung and liver tissues after treatments were stained by H&E staining and *Bouin's* fluid. Another batch of mice were received the same treatment for survival analysis until day 60.

Reporting summary

Further information on research design is available in the Nature Portfolio Reporting Summary linked to this article.

Data availability

The data generated in this study are available within the article, Supplementary Information, and Source Data. Source data are provided with this paper.

References

- Dagogo-Jack, I. & Shaw, A. T. Tumour heterogeneity and resistance to cancer therapies. *Nat. Rev. Clin. Oncol.* **15**, 81–94 (2018).
- Fisher, R., Pusztai, L. & Swanton, C. Cancer heterogeneity: Implications for targeted therapeutics. *Br. J. Cancer* **108**, 479–485 (2013).
- Meacham, C. E. & Morrison, S. J. Tumour heterogeneity and cancer cell plasticity. *Nature* **501**, 328–337 (2013).
- Phi, L. T. L. et al. Cancer stem cells (CSCs) in drug resistance and their therapeutic implications in cancer treatment. *Stem. Cells Int.* **2018**, 5416923 (2018).
- Battle, E. & Clevers, H. Cancer stem cells revisited. *Nat. Med.* **23**, 1124–1134 (2017).
- Bocci, F. et al. Toward understanding cancer stem cell heterogeneity in the tumor microenvironment. *Proc. Natl Acad. Sci. USA* **116**, 148–157 (2018).
- Visvader, J. E. & Lindeman, G. J. Cancer stem cells: Current status and evolving complexities. *Cell Stem Cell* **10**, 717–728 (2012).
- Chen, K., Huang, Y. H. & Chen, J. L. Understanding and targeting cancer stem cells: Therapeutic implications and challenges. *Acta Pharmacol. Sin.* **34**, 732–740 (2013).
- Najafi, M., Farhood, B. & Mortezaee, K. Cancer stem cells (CSCs) in cancer progression and therapy. *J. Cell. Physiol.* **234**, 8381–8395 (2019).
- Doustmihan, A. et al. Molecular targets, therapeutic agents and multitasking nanoparticles to deal with cancer stem cells: A Narrative Review. *J. Control. Release* **363**, 57–83 (2023).
- Shibu, T. & Weinberg, R. A. EMT, CSCs, and drug resistance: The mechanistic link and clinical implications. *Nat. Rev. Clin. Oncol.* **14**, 611–629 (2017).
- Shen, S. Y. et al. Nanotherapeutic strategy to overcome chemotherapeutic resistance of cancer stem-like cells. *Nat. Nanotechnol.* **16**, 104–113 (2021).
- Baumann, M., Krause, M. & Hill, R. Exploring the role of cancer stem cells in radioresistance. *Nat. Rev. Cancer* **8**, 545–554 (2008).
- Peitzsch, C., Tyutyunnykova, A., Pantel, K. & Dubrovska, A. Cancer stem cells: The root of tumor recurrence and metastases. *Semin. Cancer Biol.* **44**, 10–24 (2017).
- Shiozawa, Y., Nie, B., Pienta, K. J., Morgan, T. M. & Taichman, R. S. Cancer stem cells and their role in metastasis. *Pharmacol. Ther.* **138**, 285–293 (2013).
- Sampieri, K. & Fodde, R. Cancer stem cells and metastasis. *Semin. Cancer Biol.* **22**, 187–193 (2012).
- Oe, M. et al. Deep-Red/Near-Infrared turn-on fluorescence probes for aldehyde dehydrogenase 1A1 in cancer stem cells. *ACS Sens.* **6**, 3320–3329 (2021).
- Minn, I. et al. Red-shifted fluorescent substrate for aldehyde dehydrogenase. *Nat. Commun.* **5**, 3662 (2014).
- Anorma, C. et al. Surveillance of cancer stem cell plasticity using an isoform-selective fluorescent probe for aldehyde dehydrogenase 1A1. *ACS Cent. Sci.* **4**, 1045–1055 (2018).
- Tomita, H., Tanaka, K., Tanaka, T. & Hara, A. Aldehyde dehydrogenase 1A1 in stem cells and cancer. *Oncotarget* **7**, 11018–11032 (2016).
- Clark, D. W. & Palle, K. Aldehyde dehydrogenases in cancer stem cells: Potential as therapeutic targets. *Ann. Transl. Med.* **4**, 518 (2016).
- Jones, R. et al. Assessment of aldehyde dehydrogenase in viable cells. *Blood* **85**, 2742–2746 (1995).
- Han, J. et al. Cancer stem cell-targeted bio-imaging and chemotherapeutic perspective. *Chem. Soc. Rev.* **49**, 7856–7878 (2020).
- Yagishita, A., Ueno, T., Tsuchihara, K. & Urano, Y. Amino BODIPY-based blue fluorescent probes for aldehyde dehydrogenase 1-expressing cells. *Bioconjugate Chem.* **32**, 234–238 (2021).
- Maity, S. et al. Thiophene bridged aldehydes (TBAs) image ALDH activity in cells via modulation of intramolecular charge transfer. *Chem. Sci.* **8**, 7143–7151 (2017).
- Bearrood, T. E., Aguirre-Figueroa, G. & Chan, J. Rational design of a red fluorescent sensor for ALDH1A1 displaying enhanced cellular uptake and reactivity. *Bioconjugate Chem.* **31**, 224–228 (2020).
- Zhao, X., Liu, J., Fan, J., Chao, H. & Peng, X. Recent progress in photosensitizers for overcoming the challenges of photodynamic therapy: From molecular design to application. *Chem. Soc. Rev.* **50**, 4185–4219 (2021).
- Liu, S., Feng, G., Tang, B. & Liu, B. Recent advances of AIE light-up probes for photodynamic therapy. *Chem. Sci.* **12**, 6488–6506 (2021).
- Chen, Y. et al. Self-reporting photodynamic nanobody conjugate for precise and sustainable large-volume tumor treatment. *Nat. Commun.* **15**, 6395 (2024).
- Tang, Y. et al. Hypoxia-responsive photosensitizer targeting dual organelles for photodynamic therapy of tumors. *Small* **19**, 2205440 (2023).
- Qi, G. et al. Enzyme-mediated intracellular polymerization of AIEgens for light-up tumor localization and theranostics. *Adv. Mater.* **34**, 2106885 (2022).
- Tian, J. et al. Activatable Type I photosensitizer with quenched photosensitization Pre and Post Photodynamic Therapy. *Angew. Chem. Int. Ed.* **62**, e202307288 (2023).
- Li, X., Kolemen, S., Yoon, J. & Akkaya, E. U. Activatable photosensitizers: Agents for selective photodynamic therapy. *Adv. Funct. Mater.* **27**, 1604053 (2016).
- Tang, Y. Q., Wang, X. & Li, Q. Pyroptosis of breast cancer stem cells and immune activation enabled by a multifunctional prodrug photosensitizer. *Adv. Funct. Mater.* **34**, 2405367 (2024).
- An, J. et al. An unexpected strategy to alleviate hypoxia limitation of photodynamic therapy by biotinylation of photosensitizers. *Nat. Commun.* **13**, 2225 (2022).
- Xu, Q. et al. A self-illuminating nanoparticle for inflammation imaging and cancer therapy. *Sci. Adv.* **5**, eaat2953 (2019).
- Mao, D. et al. AIEgen-coupled upconversion nanoparticles eradicate solid tumors through dual-mode ROS activation. *Sci. Adv.* **26**, eabb2712 (2020).
- Ning, S. et al. A type I AIE photosensitizer-loaded biomimetic nanosystem allowing precise depletion of cancer stem cells and prevention of cancer recurrence after radiotherapy. *Biomaterials* **295**, 122034 (2023).
- Zhang, T. et al. Photothermal-triggered sulfur oxide gas therapy augments Type I photodynamic therapy for potentiating cancer

- stem cell ablation and inhibiting radioresistant tumor recurrence. *Adv. Sci.* **10**, 2304042 (2023).
40. Prieto-Vila, M., Takahashi, R., Usuba, W., Kohama, I. & Ochiya, T. Drug resistance driven by cancer stem cells and their niche. *Int. J. Mol. Sci.* **18**, 2574 (2017).
 41. Zhou, H., Zhang, J., Zhang, X. & Li, Q. Targeting cancer stem cells for reversing therapy resistance: Mechanism, signaling, and prospective agents. *Signal Transduct. Target. Ther.* **6**, 62 (2021).
 42. Zhang, Z., Wang, K., Mo, J., Li, X. & Yu, W. Photodynamic therapy regulates fate of cancer stem cells through reactive oxygen species. *World J. Stem Cells* **12**, 562–584 (2020).
 43. Arima, Y., Nobusue, H. & Saya, H. Targeting of cancer stem cells by differentiation therapy. *Cancer Sci.* **111**, 2689–2695 (2020).
 44. Azzi, S. et al. Differentiation therapy: Targeting human renal cancer stem cells with interleukin 15. *J. Natl. Cancer Inst.* **103**, 1884–1898 (2011).
 45. Thé, H. D. Differentiation therapy revisited. *Nat. Rev. Cancer* **18**, 117–127 (2018).
 46. Hu, J. et al. Long-term efficacy and safety of all-trans retinoic acid/arsenic trioxide-based therapy in newly diagnosed acute promyelocytic leukemia. *Proc. Natl. Acad. Sci. USA* **106**, 3342–3347 (2009).
 47. Yao, W. et al. All-trans Retinoic Acid Reduces Cancer Stem Cell-Like Cell-mediated Resistance to Gefitinib in NSCLC Adenocarcinoma Cells. *Bmc. Cancer* **30**, 315 (2020).
 48. Yang, Y. et al. Trisulfide bond-mediated doxorubicin dimeric prodrug nanoassemblies with high drug loading, high self-assembly stability, and high tumor selectivity. *Sci. Adv.* **6**, eabc1725 (2020).
 49. Sun, B. et al. Probing the impact of sulfur/selenium/carbon linkages on prodrug nanoassemblies for cancer therapy. *Nat. Commun.* **10**, 3211 (2019).
 50. Sun, B. et al. Disulfide bond-driven oxidation- and reduction-responsive prodrug nanoassemblies for cancer therapy. *Nano. Lett.* **18**, 3643–3650 (2018).
 51. Yan, M., Zuo, X. & Wei, D. Concise review: Emerging role of CD44 in cancer stem cells: A promising biomarker and therapeutic target. *Stem. Cells Transl. Med.* **4**, 1033–1043 (2015).
 52. Liu, Z. et al. A dual-targeted theranostic photosensitizer based on a TADF fluorescein derivative. *J. Control. Release* **310**, 1–10 (2019).
 53. Tang, Y. et al. Pyroptosis-Mediated Synergistic Photodynamic and photothermal immunotherapy enabled by a tumor-membrane-targeted photosensitive dimer. *Adv. Mater.* **35**, 2300232 (2023).
 54. Tang, Y., Wang, X., Chen, S. & Li, Q. Photoactivated theranostic nanomaterials based on aggregation-induced emission luminogens for cancer photoimmunotherapy. *Responsive Mater.* **2**, e20240003 (2024).
 55. Chen, Q., He, P., Wang, Z. & Tang, B. A feasible strategy of fabricating Type I photosensitizer for photodynamic therapy in cancer cells and pathogens. *ACS Nano* **15**, 7735–7743 (2021).
 56. Bahmad, H. F. et al. Sphere-formation assay: Three-dimensional in vitro culturing of prostate cancer stem/progenitor sphere-forming cells. *Front. Oncol.* **8**, 347 (2018).
 57. Lee, C. H., Yu, C. C., Wang, B. Y. & Chang, W. W. Tumorsphere as an effective in vitro platform for screening anti-cancer stem cell drugs. *Oncotarget* **7**, 1215–1226 (2016).
 58. Herreros-Pomares, A. et al. Lung tumorspheres reveal cancer stem cell-like properties and a score with prognostic impact in resected non-small-cell lung cancer. *Cell Death Dis.* **10**, 660 (2019).
 59. Heddleston, J. M. et al. Hypoxia inducible factors in cancer stem cells. *Br. J. Cancer* **102**, 789–795 (2010).
 60. Najafi, M. et al. Hypoxia in solid tumors: a key promoter of cancer stem cell (CSC) resistance. *J. Cancer Res. Clin. Oncol.* **146**, 19–31 (2020).
 61. Lee, H. E. et al. An increase in cancer stem cell population after primary systemic therapy is a poor prognostic factor in breast cancer. *Br. J. Cancer* **104**, 1730–1738 (2011).
 62. Liu, M. et al. Transcriptional profiles of different states of cancer stem cells in triple-negative breast cancer. *Mol. Cancer* **17**, 65 (2018).
 63. He, L., Wick, N., Germans, S. K. & Peng, Y. The role of breast cancer stem cells in chemoresistance and metastasis in triple-negative breast cancer. *Cancers* **13**, 6209 (2021).

Acknowledgements

We acknowledge the National University of Singapore (grant no. A-0009163-01-00), Tan Chin Tuan Centennial Professorship (grant no. E-467-00-0012-02), and National Natural Science Foundation of China (grant no. 82073779, 32000992) for funding support.

Author contributions

B. Liu and Y.P. supervised the project. B. Li and J.W.T. conceived and designed the experiments. F.Z., Z.Y.L. and C.Z.W. conducted animal experiments. S.Q.C., D.D.W., J.H.Z., W.T.S., and Y.F. T took part in the discussion and gave important suggestions. B. Li, J.W.T., B. Liu, and Y.P. co-wrote the paper. All the authors discussed, commented, and agreed on the paper.

Competing interests

The authors declare no competing interests.

Additional information

Supplementary information The online version contains supplementary material available at <https://doi.org/10.1038/s41467-024-53771-8>.

Correspondence and requests for materials should be addressed to Yuan Ping or Bin Liu.

Peer review information *Nature Communications* thanks Shipeng Ning and the other, anonymous, reviewer(s) for their contribution to the peer review of this work. A peer review file is available.

Reprints and permissions information is available at <http://www.nature.com/reprints>

Publisher's note Springer Nature remains neutral with regard to jurisdictional claims in published maps and institutional affiliations.

Open Access This article is licensed under a Creative Commons Attribution-NonCommercial-NoDerivatives 4.0 International License, which permits any non-commercial use, sharing, distribution and reproduction in any medium or format, as long as you give appropriate credit to the original author(s) and the source, provide a link to the Creative Commons licence, and indicate if you modified the licensed material. You do not have permission under this licence to share adapted material derived from this article or parts of it. The images or other third party material in this article are included in the article's Creative Commons licence, unless indicated otherwise in a credit line to the material. If material is not included in the article's Creative Commons licence and your intended use is not permitted by statutory regulation or exceeds the permitted use, you will need to obtain permission directly from the copyright holder. To view a copy of this licence, visit <http://creativecommons.org/licenses/by-nc-nd/4.0/>.

© The Author(s) 2024